Additive Manufacturing

Wire and Arc Additive Manufacturing of Thin Structures Using Metal-Cored Wire Consumables

Microstructure, mechanical properties, and experiment-based thermal model

Zidong Lin

TUDelft

Master of Science Thesis

Wire and Arc Additive Manufacturing of Thin Structures Using Metal-Cored Wire Consumables

Microstructure, mechanical properties, and experiment-based thermal model

By

Zidong Lin

in partial fulfilment of the requirements for the degree of

Master of Science
in Materials Engineering

at the Delft University of Technology,
to be defended publicly on Tuesday July 23, 2019 at 9:30 AM.

Student number: 4693965
Project duration: 1st December, 2018 - 23rd July, 2019
Supervisor: Dr.ir. M.J.M. Hermans (TUD)
Thesis committee: Dr.ir.Konstantinos Goulas (TUD)
                        Dr.ir. J.H. den Besten (TUD)
                        Dr.ir. Wei Ya (UT/RAMLAB)
                        Prof. dr. I.M. Richardson (TUD)

TUDelft   **RAMLAB**

Abstract

In recent years, Wire and Arc Additive Manufacturing (WAAM), is gaining attractions both from academia and industry, because it has the potential to substitute or complement the traditional manufacturing methods. Traditional materials and methods are reaching their limitation when demanding and special applications are considered.

The current growth in WAAM applications will boost the WAAM consumable material development in the coming future. WAAM applications mostly refer to small batch production or prototypes, which often requires special wire compositions or can benefit from tailoring the consumable composition for the desired components. On one hand, solid wire production is only economically viable when large volumes are involved. On the other hand, metal-cored wires are particularly suitable to produce tailored or small-batch consumable compositions, which is very attractive for WAAM. However, only limited research has been carried out in the use of metal-cored wires in additive manufacturing. In this research, the focus is to explore the use of metal-cored wire in WAAM applications. Two chemical compositions, one ferrous, medium carbon low steel alloy (AM-XC-45), and one non-ferrous, Stellite 6 (cobalt-based superalloy), metal-cored wires were investigated based on industrial interests at RAMLAB.

The microstructure of the WAAM AM-XC-45 thin wall was characterized using optical microscopy and scanning electron microscopy. Pearlite, ferrite, bainite, and martensite are present in the deposited wall. Columnar grains are found near the fusion line. The repeated thermal cycles cause the grains to become finer from the top to bottom layers. The mechanical properties including microhardness and tensile strength were tested and compared with the traditional processing methods like casting, milling, and forging. It showed a comparable or superior microhardness and tensile strength to the traditional process whereas the relative lower elongation of the deposited AM-XC-45 thin wall indicates that further post heat treatment is needed to improve the ductility of the part.

Stellite 6 is a cobalt-based superalloy, which has good wear and corrosion resistance and retains these properties at high temperatures. In this study, Stellite 6 metal-cored wire (WEARTECH® WT-6 GMAW-C, AWS A5.21 ERCCoCr-A) is selected and optimized to obtain results comparable to the commonly employed and more costly laser deposition, in terms of microstructure and mechanical properties. The optimal deposition parameters were developed using the S355 steel substrate, and then adopted on depositing on the AISI 420 stainless steel substrate. Characterization showed that Stellite 6 layer mainly contains Co-Cr-Fe solid solution with FCC crystal structure as the matrix and the Cr_7C_3 and Cr_3C_2 were identified in the microstructure through SEM, EDS, and XRD. These carbides can contribute to the strength. In addition, the identified Co_4W_2C carbides can contribute to the wear properties of the Stellite 6 WAAM deposits. The dilution and hardness of the WAAM deposit can reach the same level as laser deposition.

Additionally, a 3D temperature distribution model is developed by adopting the moving mesh technique to numerically study the WAAM process. The model helps to gain a better understanding of the physical phenomena (heat and mass transfer) during the WAAM deposition. The AM-XC-45 was used to validate the developed model. The simulated and experimental results were compared. The dilution and HAZ of WAAM deposited single bead was used as validation criteria. The A_1 line (1100K) simulation is in a good agreement with the experimental result. The fusion line (1800K) shows some deviation. Compared with laser deposition, the main differences between the two processes lie on the heat source, the boundary conditions, and the material responses to the process.

Acknowledgements

Contents

<div align="right">

1

</div>

<div align="right">

Introduction

</div>

1.1 Wire and Arc Additive Manufacturing (WAAM)

Additive manufacturing (AM) is a term, which refers to the manufacturing technique known to the public as "3D Printing". Additive manufacturing (AM) processes can produce 3D components directly from CAD models with dedicated software by adding materials layer by layer, offering the beneficial ability to build parts with geometric and composition complexities that could not be produced by subtractive manufacturing processes [1,2]. After a few decades of development, it has already kept the capacity to produce certain components successfully with this method. At present, the small plastic parts (Figure 1.1a) can be printed with a portable printer at home while large metal components such as a ship's propeller in an industrial framework as shown in Figure 1.1b.
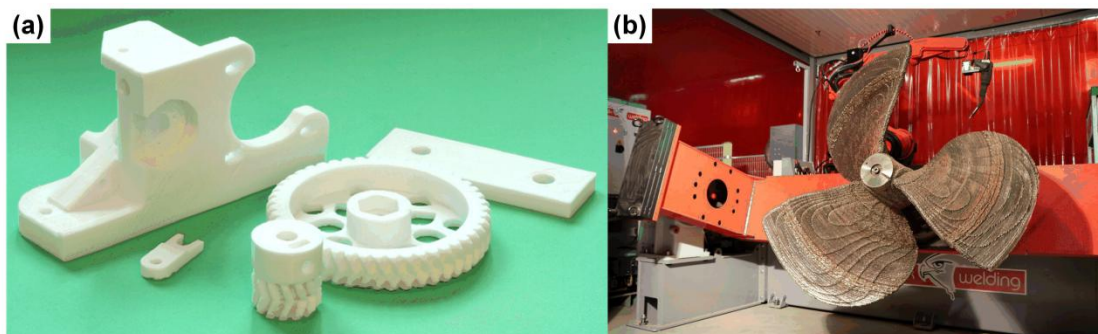
Figure 1.1 (a) 3D printed plastic parts; (b) Ship's propeller manufactured using WAAM.

Wire and Arc Additive Manufacturing (WAAM) is a one of the Direct Energy Deposition (DED) methods employed in metallic additive manufacturing (AM) with the combination of an electric arc as a heat source and wire as feeding material. WAAM has high deposition rate, high material utilization, and short production lead time [3] when compared to powder-based DED techniques. However, some drawbacks such as low surface quality, poor dimensional accuracy, inner gaps and voids [4], require attention and control during manufacturing.

The initial idea of Wire and Arc Additive Manufacturing (WAAM) can date back to 1925, when Baker [5] proposed to use arc welding to deposit metal ornaments. After the decades of development, many qualified industrial structural components such as pressure vessel and large nuclear steel parts were built up between 1970-1990 with arc deposition [6,7]. From 1990s, some automation devices such as Automatic Welding

Apparatus [8] and Shape Deposition Manufacturing [9] began to combine with arc deposition method to improve the efficiency and quality of manufacturing. Today, under the assistance of digitization, WAAM has been applied to varies fields (Figure 1.2a). More and more studies are also focused on WAAM in the recent ten years as shown in Figure 1.2b.
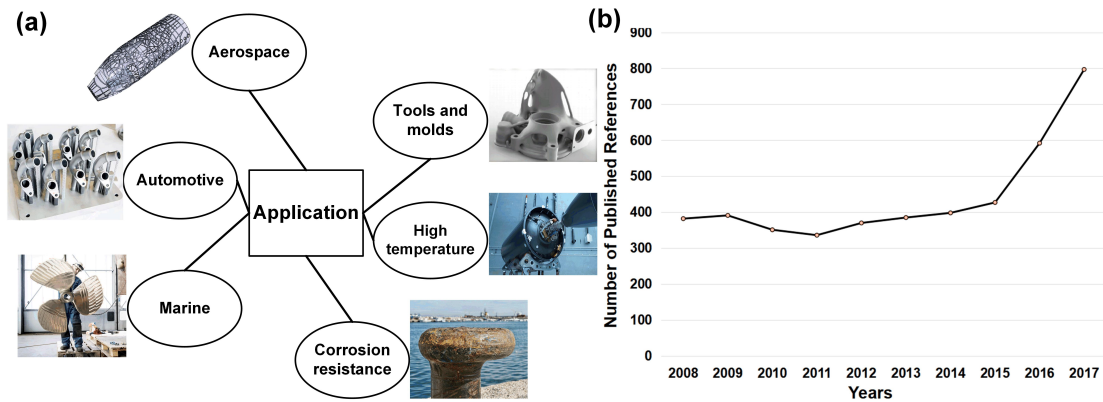
Figure 1.2 Development of WAAM, (a) application fields; (b) publication numbers in the recent ten years (Come from WorldCat, ScienceDirect and IEEE Xplore).

1.2 AM-XC-45 steel and Stellite 6 alloy

Steel is both the most widely used and most recycled metal material on earth. From stainless and high-temperature steels to flat carbon products, steel in its various forms and alloys offer different properties to meet a wide range of applications. For these reasons, as well as the metal's combination of high strength and a relatively low production cost, steel is now used in countless products.

Stellite is a type of hard-facing material, which is always used in industry. Due to the superior wear resistance no matter at moderate temperature or extremely-high temperature, it has been used to protect other metals as coating layer. Therefore, this thesis would like to explore the spectrum of application of the two materials. Based on the distinctive application requirement and material characteristic for each of them, detailed processing conditions need to be investigated respectively.
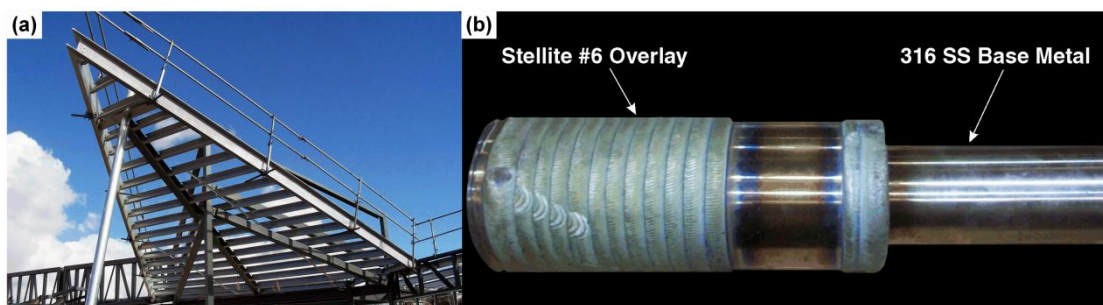
Figure 1.3 (a) Heavy loaded AM-XC-45 steel structure; (b) Stellite 6 surface hardener.

AM-XC-45 steel, a medium carbon structural steel, is typically used to produce heavy loaded structure and aerospace parts, as shown in Figure 1.3a. Due to the high average carbon content (0.42 - 0.45%), it keeps good mechanical properties like high tensile and yield strength (over 600 MPa and 355 MPa). However, the traditional welding of medium carbon steel is very challenging, meaning that the part normally needs post-processing to lower the possibility of defects caused by poor ductility [10]. Such post-processing is energy and time intensive, which is not preferred.

Stellite 6 is the most widely used type of cobalt-based super alloy, with nominal composition Co-28Cr-4.5W-1.2C. It is regarded as the industry standard for general-purpose wear resistance applications, has excellent resistance to many forms of mechanical and chemical degradation over a wide temperature range, and retains a reasonable level of hardness up to 500°C (930°F). Stellite 6 is suited to a variety of hard-facing processes as a surface hardener (Figure 1.3b) and has been used in many harsh conditions such as pump shafts, erosion shields, and rolling couples. However, its high hardness increases the possibility of cracking during the manufacturing, which needs some care when it is applied.

1.3 Thermal model

Thermal model is mainly used to calculate the temperature distribution during the deposition process. In multi-beads WAAM deposition, overlap ratio (horizontal direction) and overstep distance (vertical direction) are important for the quality of parts. Both are much dependent on the single bead characteristic. Therefore, in this research, a 3D thermal model for single bead is constructed using moving mesh technique. It helps to gain a better understanding of the physical phenomenon (heat and mass transfers) occurring during WAAM process.

1.4 Structure of the thesis

There are 7 chapters in this thesis. Chapter 1 is the general introduction. Chapter 2 is state of art and it gives a brief overview of the research that has been performed and the main outcomes which is relevant to current research. The experimental setup, assumptions, results, discussion and conclusions found in literature are also introduced in this chapter. Chapter 3 gives a detailed explanation on the different experimental setup, materials used in this research, experimental methodologies equipment and methods used for the sample preparation and examination. Chapter 4 introduces the study on WAAM depositing of AM-XC-45 using metal-cored wire. Chapter 5 shows the study on WAAM deposition of Stellite 6 using metal-cored wire. Chapter 6 introduces 3D thermal modelling of WAAM deposition process. Chapter 7 provides the conclusions of this master thesis and the recommendations for future research.

Bibliography

[1] Guo N, Leu M C. Additive manufacturing: technology, applications and research needs[J]. Frontiers of Mechanical Engineering, 2013, 8(3): 215-243.

[2] ASTM Committee F42 on Additive Manufacturing Technologies, ASTM Committee F42 on Additive Manufacturing Technologies. Subcommittee F42. 91 on Terminology. Standard terminology for additive manufacturing technologies[M]. ASTM International, 2012.

[3] Williams S W, Martina F, Addison A C, et al. Wire+ arc additive manufacturing[J]. Materials Science and Technology, 2016, 32(7): 641-647.

[4] Ding D, Pan Z, Cuiuri D, et al. A practical path planning methodology for wire and arc additive manufacturing of thin-walled structures[J]. Robotics and Computer-Integrated Manufacturing, 2015, 34: 8-19.

[5] Ralph B. Method of making decorative articles: U.S. Patent 1,533,300[P]. 1925-4-14.

[6] Yan L. Wire and arc addictive manufacture (WAAM) reusable tooling investigation[J]. 2013.

[7] Colegrove P, Williams S. High deposition rate high quality metal additive manufacture using wire+ arc technology[J]. Cranfield University, 2013.

[8] Acheson R. Automatic welding apparatus for weld build-up and method of achieving weld build-up: U.S. Patent 4,952,769[P]. 1990-8-28.

[9] Merz R, Prinz F B, Ramaswami K, et al. Shape deposition manufacturing[C]//1994 International Solid Freeform Fabrication Symposium. 1994.

[10] Mercelis P, Kruth J P. Residual stresses in selective laser sintering and selective laser melting[J]. Rapid prototyping journal, 2006, 12(5): 254-265.

Literature Review

2.1 WAAM Deposition Systems

The basic WAAM deposition systems are built on traditional welding systems, including Gas Metal Arc Welding (GMAW), Gas Tungsten Arc Welding (GTAW) and Plasma Arc Welding (PAW), which is summarized in Table 2.1. Both GMAW and Plasma have relative high heat input. But GMAW has a higher degree of automation while the equipment and start-up cost of Plasma is high. Therefore, for industrial applications, GMAW is preferred. When large scale and high deposition are not required, GTAW based system could be a candidate as its low price, good ability of deposition on complicated shapes with different dimensions, availability of a wide range of materials, and good arc stability [1].

Table 2.1 The comparison of basic WAAM deposition systems.

Deposition systems	Arc form	Deposition rate (kg/h)	Post-processing	Stability	Cost	Heat input	Thermal efficiency (%)
GMAW-based	GMAW	3-4	Independent system	Splash	Low	High	84
GTAW-based	GTAW	1-2		Good	Low	Low	67 [2]
PAW-based	Plasma	2-4		Good	High	High	47

Based on the these commonly used basic welding systems, researchers made efforts to improvements, which are mainly focused on reducing production costs, improving deposition quality and deposition efficiency to tailor for WAAM. An overview of the improved deposition systems is shown in Figure 2.1 [3-11].

Disadvantages	Improved deposition systems	Improvements
Bad stability of arc	Double-electrode system	Higher deposition rate
	Double wire feeding system	Higher deposition rate Finer grain
High cost; Limitation of part dimension	3D Micro deposition system	Less defect
Bad effect of polarity occupancy ratio (AC)	Variable Polarity system	
More maintenance; skilled programmer; High cost	CNC hybrid system	Less/no post-processing More accurate shape

Figure 2.1 An overview of the improved deposition systems.

2.2 WAAM deposition Path Planning

In WAAM system, path planning plays an important role for controlling deposition process. As an indispensable procedure for WAAM, a good tool path planning can improve surface waviness (peak to valley distance) and deposition accuracy of the part. Some path planning examples are shown in Table 2.2. Therefore, according to specific applications, the optimal path planning method should be considered based on the requirements, such as quality, dimension, shape, cost, etc.

Table 2.2 Comparison of different path planning methods.

Path planning	Features	Path morphology	Literature
Raster	Simple data structure; Cheap; Easy to analyze; Outline accuracy of part is poor		[12,13]
Zigzag	Low cost; Start and stop points decrease; High efficiency caused by combination of line; Outline accuracy of part is poor		[14,15]
Contour	High efficiency due to less moving; Predict the geometry issue; Numerous closed curves cause much start and stop points		[16,17]
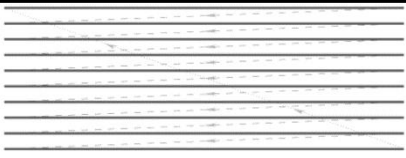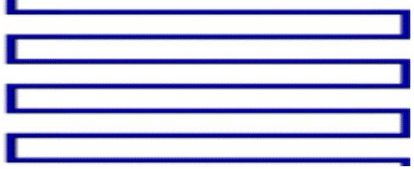
6

Hybrid (Contour + zigzag)	High surface accuracy and quality; High building efficiency		[18]
MAT-based	Work from inside to outside that generate void-free deposition paths; Paths can entirely fill the interior region; Work for any complex geometry		[19]
Adaptive MAT	Cost save compared with MAT-based; Improve accuracy and efficiency by varying step-over distances automatically		[20]
Spiral	Simple data structure; Adaptable for numerically controlled (NC) machining; Only be used in special geometrical models		[21]
Continuous	Fill any arbitrarily shaped area; Number of welding passes is reduced; Number of start and stop points are minimized		
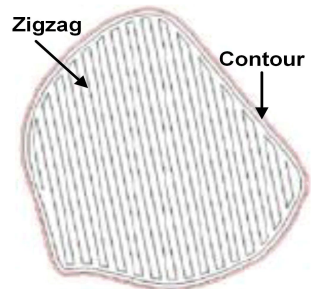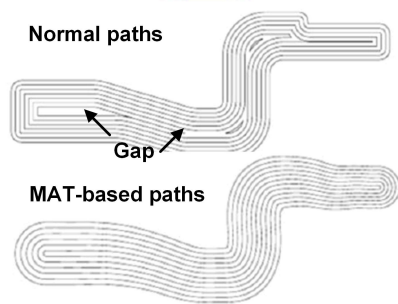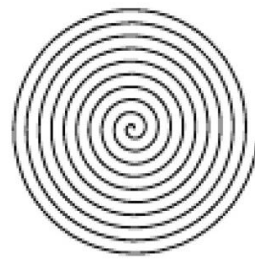
2.3 WAAM Materials

In principle, any weldable metallic material can be applied in the WAAM deposition. This section provides an overview of the typical metallic materials used in WAAM.

2.3.1 Traditional materials

7

The most commonly used materials in WAAM are still traditional welding standard filler material including steel, aluminium and titanium alloys. They are summarized and listed in Table 2.3. The typical microstructure including (phases, grain shape) and mechanical properties (hardness, ultimate tensile strength, and elongation) of different materials used in WAAM deposited part are illustrated. For the same material, different deposition systems could change the microstructure and mechanical properties of the WAAM deposited part.

Table 2.3 Traditional materials used in WAAM.

Material		Deposition system	Microstructure	Hardness (HV)	UTS (MPa)	Elongation (%)	Literature
Steel alloys	Maraging steel	PAM	Cellular and dendritic martensitic	340-440	1048	17	[22]
		CMT	Cellular dendritic martensitic and more oxides layers				
	Mild steel	GMAW	Ferrite and pearlite at the grain boundaries	125-160	460	34-38	[23]
	C-Mn steel	GTAW	Fine-grained polygonal ferrite with small fractions of Widmanstätten/ bainitic ferrite	/	500	22-25	[24]
	Stainless steel	GMAW	Skeletal and lathy δ-ferrite	/	499.11 ± 6.76	28.3	[25]
Aluminum alloys	AA2219	CMT	Coarse columnar grain structure	68	260	16	[26]
		CMT-VP	Equiaxed grains were distributed in the fusion zone	70-80	265	/	
		CMT-Pulse	Coarse columnar grain structure	68-75	265	/	
		CMT-P-VP	Mixture of coarse columnar grain and finer equiaxed grain; Cu Second phase particles scattered evenly	65-70	280	19	

Titanium alloys	Ti-6Al-4V	GTAW	Columnar prior β grains + Widmanstätten α/β	300-350	965	9	[27]
				/	918	14.8	[28]
			Widmanstätten α + banded coarsened lamella α	337	939	14	[29]
			Basket weave + α-phase lamella structures				
		PAM	Prior columnar β + martensite α' + fine basket-weave structure	270-360	968	11.5	[30]
		Pulsed PAM	Prior columnar β + martensite α'	345-365	988	7	[31]

Apart from the materials introduced above, some other metals have also been investigated for potential application for WAAM process, such as magnesium alloy AZ31 for automotive applications [32], Fe/Al intermetallic compounds [33] and Al/Ti [34] compounds, as well as the bimetallic steel/nickel [35] WAAM parts for the aeronautic industry. However, more traditional metals are still needed to be further studied.

2.3.2 Metal-cored wires

Metal-cored wire is a composite tubular filler material, having a metal sheath and a core filled by various of powdered materials. Compared to flux-cored wires [36], the content of fluxing agents is reduced in metal-cored wires, which is beneficial for controlling the formation of inclusion in the weld metal. The alloy composition of metal-cored wires can be further optimized to reduce the sensitivity towards certain weld defects, such as cracking and porosity. Metal-cored wires are also suitable for repairing or manufacturing a spare component with a chemical composition that does not match the existing welding consumables. WAAM applications can benefit significantly from this flexibility introduced by metal-cored wires.

Metal-cored wires consisting of a solid sheath and a powder core (Figure 2.2), do not offer the rigidity as solid wires [37]. During a deposition, metal-cored wires conduct current only through the sheath, which results in higher current density. The powder inside the sheath is melted by the arc, resulting in the formation of powder lance towards the base. However, there is no energy transfer via the powder lance, which means that less energy is required to melt the same volume of the metal-cored wire than the solid wire. Due to this, the heat input in the WAAM component is reduced. Additionally, to obtain similar deposition characteristics, i.e., bead shape, aspect ratio, and deposition speed, a metal-cored wire requires comparably lower current than a solid wire.

Due to these advantages of metal-cored wires mentioned above it attracted the attention of many researchers and institutions in the past two decades [38,39]. The studies so far indicate that metal-cored wires are a good candidate for using in additive manufacturing. Nevertheless, the application of only limited metal-cored wires in WAAM has been reported [40,41].
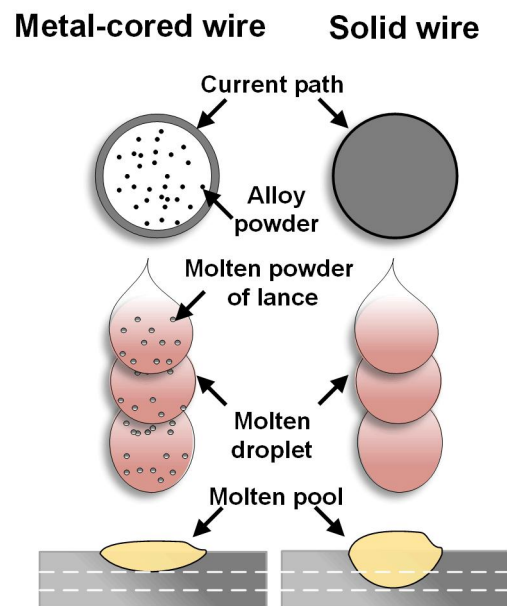
Figure 2.2 Comparison between metal-cored wire and metal solid wire.

2.4 WAAM deposition using the medium carbon steel and Stellite 6

2.4.1 WAAM deposition using medium carbon steel (AM-XC-45)

There is few reported on the additive manufacturing of the AM-XC-45 steel grade using WAAM. Aiming for a better understanding in the microstructure evolution and mechanical properties of WAAM deposited AM-XC-45, it is helpful to familiar with the AISI 1045 weld material properties, which chemical composition is close to AM-XC-45 using is our study. However, AISI 1045 is more often used as substrate instead of weld consumable. As the WAAM process is rooted from GMAW process, the relevant arc welding and heat treatment of AISI 1045 can be helpful.

J. J. Coronado and C. Cerón [42] investigated the microstructure and fracture of the AISI 1045 joints obtained with submerged arc welding using flux-cored wire. It was found that pearlite, ferrite, and some MnS inclusions formed. It showed a ductile fractures with sulfide inclusions inside large and spherical dimples. I. Akhyar and M. Sayuti [43] studied the effect of hardening and of tempering processes toward hardness, microstructure, and cracking of the AISI 1045. The result showed that the hardness values properties increased with increase of temperature, except at 1000 °C. T.A. Palmer and J.W. Elmer [44] directly observed the formation and growth of austenite from pearlite and allotriomorphic ferrite in AISI

1045 arc weld. With rapid heating, cementite does not completely dissolve before the base metal ferrite is transformed, and a second austenite constituent forms. These two austenite constituents exist up to 1400 °C before a single homogeneous austenite phase is produced.

2.4.2 WAAM deposition of Stellite 6

From the literatures, it can be concluded that the microstructure of deposited Stellite 6 is composed of Co-rich dendrite and Cr-rich eutectic carbides. Two main types of carbides have been reported for cobalt-based alloys. They are chromium-rich carbides (Cr_3C_2, Cr_7C_3 and $Cr_{23}C_6$) and refractory-element-rich carbides (M_6C and MC) [45]. These carbides contribute to a high hardness, corrosion resistance, and wear resistance of the Stellite 6 deposits.

The hardness of Stellite 6 deposits is normally higher than 500 HV [46]. The layer coated by laser deposition can reach a higher hardness (above 600 HV [46]), due to the faster cooling rate achieved. However, high hardness could increase the possibility of cracking, especially in the interface due to the stress concentration can be developed as thermal mismatch exists [47]. Z. Li et al. [48] studied the effect of post heat treatment on the hardness of the WAAM Stellite 6 parts. They found that both WAAM part and stress relief annealing component is ~7-8 HRC higher than casting part. Therefore, stress relief annealing has no obvious effect on improving the hardness.

2.5 The temperature field simulation

Welding is one of the most commonly used manufacturing processes, such as maritime, automotive, shipbuilding, and nuclear industries, among others. However, the occurrence of undesirable microstructure, thermal stress concentration, and thermal distortion increase the possibility of structural failure significantly [49]. Many kinds of simulation methods have been developed to understand and eventually avoid these failures.

In 1940s, the modelling of temperature field during welding was initiated by Rosenthal [50] and Rykalin [51], who assumed point and linear heat sources. Since then, simulation becomes a topic in academic society. Ruifeng Li et al. [52] used heat source model with Gaussian distribution to simulate the temperature and developed stress field for laser deposited Ni coatings. Although the simulated bead profile was comparable with experimental result, deviation observed at the boundary between HAZ and base. Eduardo José Fernandes Rocha et al. [53] studied the temperature field generated during the deposition of steel weld bead using the Double-Ellipsoid model. However, simulated boundary between HAZ and base deviates up to 22.46%. V Dhinakaran et al. [54] simulated arc welding of Ti alloy process using a heat source model with Gaussian distribution. It also noticed that there is mismatch in the bead geometry. This indicates that the

physical coupling, such as temperature and geometry, during simulation still to be improved. Ya et al. [55] used moving mesh technique to overcome this by coupling laser material interactions, the temperature distribution and geometrical changes in the simulation of a 2D laser deposition process, which shows that the potential of adopting such techniques for AM simulation as their experimental and simulation results agree well with each other.

2.6 Conclusions

Through the state of art study, it provides the knowledge bases for further exploring the research topics proposed in this master thesis. As the flexibility provided by metal cored wire, it offers the potential for tailored AM materials development with desirable properties including process and resulting microstructure. The research on the WAAM deposition of AM-XC-45 is novel. The research on the WAAM deposition of Stellite 6 will be beneficial for industries who cannot afford the expensive laser solution. The adaptation of moving mesh techniques can be helpful for a better understanding the additive manufacturing process in WAAM.

Bibliography

[1] Norrish J. Advanced welding processes[M]. Elsevier, 2006.

[2] DuPont J N, Marder A R. Thermal efficiency of arc welding processes[J]. Welding Journal-Including Welding Research Supplement, 1995, 74(12): 406s.

[3] Y. Zhang, M. Jiang, W. Lu, Double electrodes improve GMAW heat input control, Welding Journal 83(11) (2004) 39-41.

[4] K. Li, J. Chen, Y. Zhang, Double-electrode GMAW process and control, WELDING JOURNAL-NEW YORK- 86(8) (2007) 231.

[5] Y. Feng, B. Zhan, J. He, K. Wang, The double-wire feed and plasma arc additive manufacturing process for deposition in Cr-Ni stainless steel, Journal of Materials Processing Technology 259 (2018) 206-215.

[6] H. Wang, W. Jiang, J. Ouyang, R. Kovacevic, Rapid prototyping of 4043 Al-alloy parts by VP-GTAW, Journal of Materials Processing Technology 148(1) (2004) 93-102.

[7] M. Yarmuch, B. Patchett, Variable AC polarity GTAW fusion behavior in 5083 aluminum, WELDING JOURNAL-NEW YORK- 86(7) (2007) 196.

[8] T. Horii, M. Ishikawa, S. Kirihara, Y. Miyamoto, N. Yamanaka, Development of Freeform Fabrication of Metals by Three Diminsional Micro-Welding, Solid State Phenomena, Trans Tech Publ, 2007, pp. 189-194.

[9] J. Li, H. Li, H. Wei, Y. Ni, Effect of pulse on pulse frequency on welding process and welding quality of pulse on pulse MIG welding-brazing of aluminum alloys to stainless steel, The International Journal of Advanced Manufacturing Technology 87(1-4) (2016) 51-63.

[10] P. Almeida, S. Williams, Innovative process model of Ti–6Al–4V additive layer manufacturing using cold metal transfer (CMT), Proceedings of the twenty-first annual international solid freeform fabrication symposium, University of Texas at Austin, Austin, TX, USA, 2010.

[11] J. Prado-Cerqueira, J. Diéguez, A. Camacho, Preliminary development of a wire and arc additive manufacturing system (WAAM), Procedia Manufacturing 13 (2017) 895-902.

[12] G. Boothroyd, P. Dewhurst, W.A. Knight, Product design for manufacture and assembly, M. Dekker, New York, 1994.

[13] M.R. Dunlavey, Efficient polygon-filling algorithms for raster displays, ACM Transactions on Graphics 2 (1983) 10.

[14] S.C.P.a.B.K. Choi, Tool-path planning for direction-parallel area milling, Computer- Aided Design 32 (2000) 9.

[15] V.S. V. Rajan, and K. A. Tarabanis, The optimal zigzag direction for filling a two dimensional region, Rapid Prototyping Journal 7 (2001) 12.

[16] Y. Yang, H. Loh, J. Fuh, Y. Wang, Equidistant path generation for improving scanning efficiency in layered manufacturing, Rapid Prototyping Journal 8(1) (2002) 30-37.

[17] Y. Zhang, Y. Chen, P. Li, A.T. Male, Weld deposition-based rapid prototyping: a preliminary study, Journal of Materials Processing Technology 135(2-3) (2003) 347-357.

[18] G. Jin, W. Li, L. Gao, An adaptive process planning approach of rapid prototyping and manufacturing, Robotics and Computer-Integrated Manufacturing 29(1) (2013) 23-38.

[19] J.-H.K.a.F.B. Prinz, Optimal motion planning for deposition in layered manufacturing, 1998 ASME Design Engineering Technical Conferences, Atlanta, Georgia, USA, 1998, p. 10.

[20] W.L. G. Jin, and L. Gao, An adaptive process planning approach of rapid prototyping and manufacturing, Robotics and Computer-Integrated Manufacturing 29 (2013) 16.

[21] J. Vora, V.J. Badheka, Advances in Welding Technologies for Process Development, CRC Press2019.

[22] J.D. Xiangfang Xu, Supriyo Ganguly, Chenglei Diao, Stewart Williams, Oxide accumulation effects on wire + arc layer-by-layer additive manufacture process, Journal of Materials Processing Technology 252 (2018) 12.

[23] G.Z. C.V. Haden, F.M. Carter III, C. Ruhl, B.A. Krick, D.G. Harlow, Wire and arc additive manufactured steel: Tensile and wear properties, Additive Manufacturing 16 (2017) 9.

[24] Niyanth Sridharana, Mark W. Noakesb, Andrzej Nyczb, Lonnie J. Loveb, Ryan R. Dehoffa,, S.S. Babub, On the toughness scatter in low alloy C-Mn steel samples fabricated using wire arc additive manufacturing, Materials Science & Engineering A 713 (2018) 10.

[25] C.V.H. J.V. Gordona, H.F. Nied, R.P. Vinci, D.G. Harlow, Fatigue crack growth anisotropy, texture and residual stress in austenitic steel made by wire and arc additive manufacturing, Materials Science & Engineering A 724 (2018) 8.

[26] C. Zhang, Y. Li, M. Gao, X. Zeng, Wire arc additive manufacturing of Al-6Mg alloy using variable polarity cold metal transfer arc as power source, Materials Science and Engineering: A 711 (2018) 415-423.

[27] O.v.d.B. Bernd Baufeld, Rosemary Gault, Microstructure of Ti-6Al-4V specimens produced by shaped metal deposition, International Journal of Materials Research 100 (2009) 7.

[28] S.W. Fude Wang, Paul Colegrove, Alphons A. Antonysamy, Microstructure and Mechanical Properties of Wire and Arc Additive Manufactured Ti-6Al-4V, Metallurgical and Materials Transactions A 44 (2013) 10.

[29] E.B. Bernd Baufeld, Omer van der Biest, Wire based additive layer manufacturing: Comparison of microstructure and mechanical properties of Ti-6Al-4V components fabricated by laser-beam deposition and shaped metal deposition, Journal of Materials Processing Technology 211 (2011) 13.

[30] L.Y. Lin J, Liu Y, Sun Z, Wang K, Li Z, et al, Microstructural evolution and mechanical property of Ti-6Al-4V wall deposited by continuous plasma arc additive manufacturing without post heat treatment, Journal of the Mechanical Behavior of Biomedical Materials 69 (2017) 11.

[31] Y.H.L. J.J. Lin, Y.X. Liu, B.S. Xu, Z. Sun, Z.G. Li, Y.X. Wu, Microstructural evolution and mechanical properties of Ti-6Al-4V wall deposited by pulsed plasma arc additive manufacturing, Materials and Design 102 (2016) 11.

[32] Z.Y. Guo J, Liu C, Wu Q, Chen X, and Lu J, Wire Arc Additive Manufacturing of AZ31 Magnesium Alloy: Grain Refinement by Adjusting Pulse Frequency, Materials 9 (2016) 10.

[33] Z.P. Chen Shen, Yan Ma, Dominic Cuiuri, Huijun Li, Fabrication of iron-rich Fe-Al intermetallics using the wire-arc additive manufacturing process, Additive Manufacturing 7 (2015) 7.

[34] D.C. Yan Ma, Chen Shen, Huijun Li, Zengxi Pan, Effect of interpass temperature on in-situ alloying and additive manufacturing of titanium aluminides using gas tungsten arc welding, Additive Manufacturing 8 (2015) 7.

[35] Takeyuki Abea, Hiroyuki Sasaharab, Dissimilar metal deposition with a stainless steel and nickel-basedalloy using wire and arc-based additive manufacturing, Precision Engineering 45 (2016) 9.

[36] Nikodym A. Flux-cored wire formulation for welding: U.S. Patent 6,855,913[P]. 2005-2-15.

[37] Boothroyd G. Product design for manufacture and assembly[J]. Computer-Aided Design, 1994, 26(7): 505-520.

[38] Klimpel A, Dobrzański L A, Janicki D, et al. Abrasion resistance of GMA metal cored wires surfaced deposits[J]. Journal of materials processing technology, 2005, 164: 1056-1061.

[39] Arivazhagan B, Kamaraj M. Metal-cored arc welding process for joining of modified 9Cr-1Mo (P91) steel[J]. Journal of Manufacturing Processes, 2013, 15(4): 542-548.

[40] Gualco A, Svoboda H G, Surian E S, et al. Effect of welding procedure on wear behaviour of a modified martensitic tool steel hardfacing deposit[J]. Materials & Design, 2010, 31(9): 4165-4173.

[41] Corus. European structural steel standard EN 10025-2:2004. Available online: https://www.tf.unikiel.de/matwis/amat/iss/kap_9/articles/en_steel_standards.pdf (accessed on 8 June 2019).

[42] Coronado J J, Cerón C. Fracture mechanisms of CTOD samples of submerged and flux cored arc welding[J]. Theoretical and Applied Fracture Mechanics, 2010, 53(2): 145-151.

[43] Akhyar I, Sayuti M. Effect of heat treatment on hardness and microstructures of AISI 1045[C]//Advanced Materials Research. Trans Tech Publications, 2015, 1119: 575-579.

[44] Palmer T A, Elmer J W. Direct observations of the formation and growth of austenite from pearlite and allotriomorphic ferrite in a C–Mn steel arc weld[J]. Scripta materialia, 2005, 53(5): 535-540.

[45] Rebouças Filho P P, da Silveira Cavalcante T, de Albuquerque V H C, et al. Measurement of welding dilution from images using active contours[C]//SEECCM 2009-2nd South-East European Conference on Computational Mechanics. 2009.

[46] Kusmoko A, Li H. Measuring Dilution and Wear for Stellite 6 Deposited on P22 Steel Substrate by Laser Cladding[J]. Applied Science and Mathematics, 2016, 3: 18-21.

[47] Sheikh-Ahmad J, Chipalkati P. Effect of cutting edge geometry on thermal stresses and failure of diamond coated tools[J]. Procedia Manufacturing, 2015, 1: 663-674.

[48] Li Z, Cui Y, Wang J, et al. Characterization of Microstructure and Mechanical Properties of Stellite 6 Part Fabricated by Wire Arc Additive Manufacturing[J]. Metals, 2019, 9(4): 474.

[49] K. Masubuchi, Analysis of Welded Structures: Residual Stresses, Distortion, and Their Consequences International Series on Materials Science and Technology, Oxford and New York: Pergamon Press, 1980.

[50] D. Rosenthal, Mathematical theory of heat distribution during welding and cutting, Welding journal 20 (1941) 220-234.

[51] N. Rykalin, Thermal basics of welding, AN SSSR, Moskva (1947).

[52] R. Li, Y. Qiu, Q. Zheng, B. Liu, S. Chen, Y. Tian, Finite Element Simulation of Temperature and Stress Field for Laser Cladded Nickel-Based Amorphous Composite Coatings, Coatings 8(10) (2018) 336.

[53] E.J.F. Rocha, T.d.S. Antonino, P.B. Guimarães, R.A.S. Ferreira, J.M.A. Barbosa, J. Rohatgi, modelling of the temperature field generated by the deposition of weld bead on a steel butt joint by FEM techniques and thermographic images, Materials Research 21(3) (2018).

[54] V. Dhinakaran, N.S. Shanmugam, K. Sankaranarayanasamy, Experimental investigation and numerical simulation of weld bead geometry and temperature distribution during plasma arc welding of thin Ti-6Al-4V sheets, The Journal of Strain Analysis for Engineering Design 52(1) (2017) 30-44

[55] W. Ya, B. Pathiraj, S. Liu, 2D modelling of clad geometry and resulting thermal cycles during laser cladding, Journal of materials processing technology 230 (2016) 217-232.

<div align="right">

3

</div>

Experimental setup, materials and methods

In this study, parametric investigation of WAAM depositing AM-XC-45 and Stellite 6 metal-cored wires were carried out, aiming to get the optimal deposition parameter for the subsequent part building and surface deposition. Therefore, the experimental setup and the materials used were introduced. In addition, the scientific and engineering approaches employed in this study are also introduced in this chapter.

3.1. Experimental setup
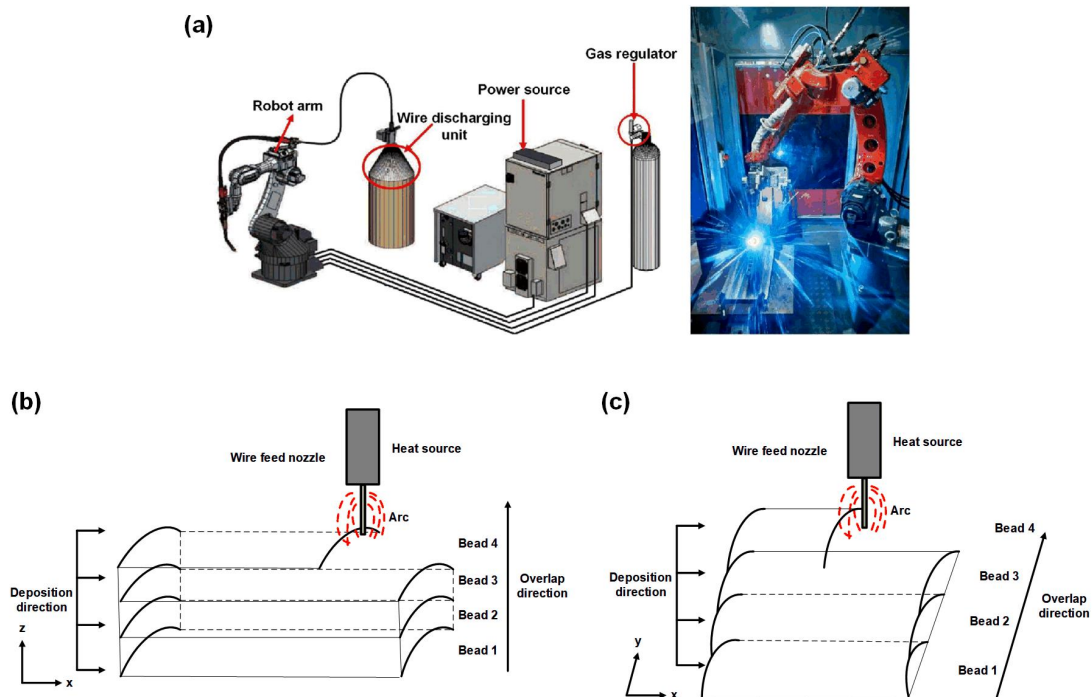
Figure 3.1 (a) Physical map of welding robot; (b) Schematic diagram of AM-XC-45 deposition process; (c) Schematic diagram of Stellite 6 deposition process.

In this study, the deposition was carried out using a Panasonic robotic arm and a power source integrated by Valk Welding, which is shown in Figure 3.1a. The software used for designing the deposition tool path was Autodesk PowerMill (Autodesk B.V, Hoofddorp, Netherlands). Figure 3.1b and 3.1c show the planned

experiment setup of the AM-XC-45 and Stellite 6 deposition paths separately, from which it can be seen that a single bead wall was deposited using AM-XC-45 while a thin single layer was deposited using Stellite 6. For AM-XC-45, the wall was air-cooled after deposition of each layer until the top surface was measured to be at room temperature. For Stellite 6, the deposition was continuous, which means no intermediate cooling between the deposition of adjacent layers. In addition, the torch was always positioned perpendicular to the workpiece (PA position).

3.2. Experimental materials

In this study, S355 structural steel [1] and AISI 420 stainless steel base plate of $250 \times 60 \times 10$ mm^3 were used. AM-XC-45 (equivalent to steel standard AFNOR, NF A37-502) and WEARTECH® WT-6 (equivalent to Stellite 6) metal-cored wire with the diameter of 1.2 mm were employed as filler materials. The chemical composition of materials used in this work was given in Table 3.1 and 3.2. Two kinds of gases were used for AM-XC-45 and stellite 6 deposition respectively, which can be seen in Table 3.3. Acetone $((CH_3)_2CO)$ solution was used to clean the base plate before deposition starts.

Table 3.1 Chemical composition of the steel substrates [wt.%].

	C	Si	Mn	P	Cu	Fe	Cr
AISI S355	0.2	0.55	1.6	0.025	0.55	Bal.	/
AISI 420	<0.15	<1.0	<1.0	<0.04	/	Bal.	12.0-14.0

Table 3.2 Chemical composition of the wire [wt.%].

	Cr	W	C	Ni	Mo	Fe	Si	Mn	Co
Stellite 6 wire, (WEARTECH® WT-6 GMAW-C, AWS A5.21 ERCCoCr-A)	28.2	4.1	1.2	0.3	0.1	3.9	0.5	0.8	Bal.
Stellite 6 ((SF)A 5.21 ERCoCr-A)	30	4-5	1.2	<3.0	<1.0	<3.0	<2.0	/	Bal.

Table 3.3 Gases used in this study.

Name	Composition	Flow rate	Depositing material

Ferromaxx® plus	20%He, 12%CO$_2$, 68% Ar	18 [L min^{-1}]	AM-XC-45
Alumax	30% He, 70% Ar		Stellite 6

3.3. Experimental methods

3.3.1 Single bead characteristics

A schematic cross section of a single bead bonded on a substrate is shown in Figure 3.2. Figure 3.2a is a schematic and Figure 3.2b shows an actual deposited bead. It indicates the characteristics of a single bead, which include bead height (H_b), bead width (W_b), bead area (A_c) above the substrate surface, dilution zone (A_{mix}) below the substrate surface, penetration depth (d_m), and heat affected zone (HAZ).

Dilution is defined as the mixing ratio between the coating and substrate material. In principle, dilution refers to elements ratio of the mixing between substrate and the coating materials in the solidified melt. Schneider [2] has shown that such elements ratio can be correlated to the bead geometry. Hence, the deposited bead width over bead height was defined as aspect ratio ($AR = W_b / H_b$) according to Abbas and West [3], which is used in this research. The geometrical dilution is defined as the penetration depth over the sum of the penetration depth and bead height ($D_d = 100\% \times d_m / (d_m + H_b)$). The chemical dilution is defined as $D_c = (C_{deposit} - C_{wire}) / C_{wire}$ [4].
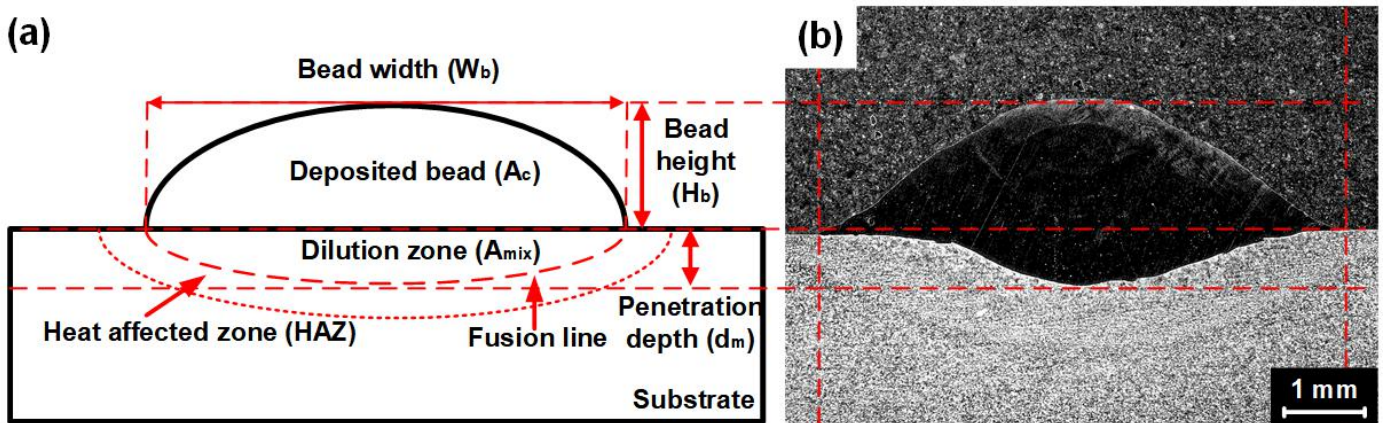
Figure 3.2 Stellite cross section, (a) Schematic drawing; (b) as deposited Stellite 6.

3.3.2 Ramping deposition strategy

Aiming to investigate the optimal deposition condition for both AM-XC-45 and Stellite 6 wires, many single bead deposition tests are to be performed, which will be time and material consuming if following traditional welding tests with single parameter variation for each bead. Ramping deposition strategy [5] is an alternative,

which is a cost-saving and effective method. It can combine different processing conditions within the same deposited bead without redundant tests [5]. Besides, the effect of different deposition parameters on the bead geometry is more intuitive and apparent for comparison. Therefore, the optimal deposition condition with an appropriate width to height ratio [6] can be selected quickly. The schematic of the ramping deposition is shown in Figure 3.3.
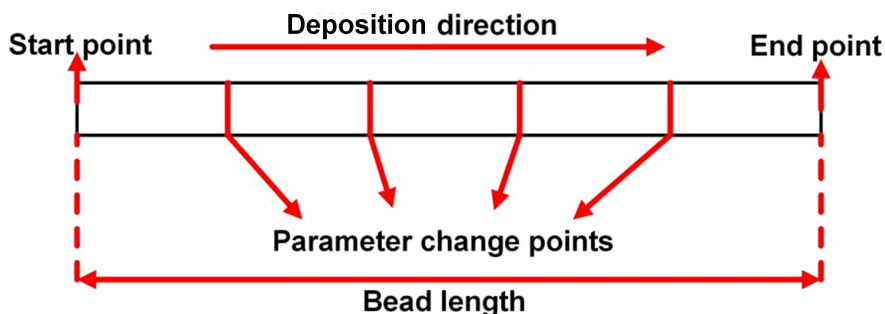
Figure 3.3 Schematic of ramping deposition.

3.3.3 Overlap experiments

In addition, overlap experiments were performed by overlapping beads through the lateral displacement of the robot arm (d_r) to determine the optimal overlap ratio (OR=100%×(W_b - d_r)/ W_b), as shown in Figure 3.4. Overlap ratio values were determined based on the dimensions of the bead. The selection was aiming to avoid inter-run-porosity at the weld toe (bead too small) and deep valleys (bead too big) [7]. The overlapping deposition in this study consisted of seven overlapped beads. The length of each bead was 20 mm. The deposition process was continuous, which means that there was no inter-pass cooling after depositing each bead. After the deposition, the layer was air cooled to room temperature. Samples were cut and prepared according to standard metallurgical procedures for further analysis.
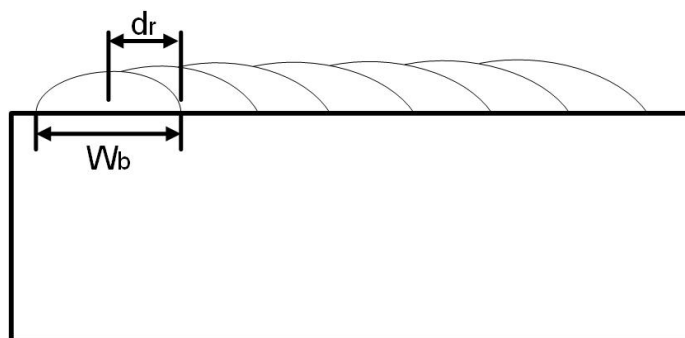
Figure 3.4 Schematic view of overlapped bead tracks.

3.3.4 Imaging method

For learning about the process of bead height growth, the C300 Cavitar Welding Camera was used to observe the deposition of the single bead. In this way, the molten droplet transfer, dimension of molten pool, and the start / stop points of material addition were studied, which were used in the following simulation process.

3.3.5 Sample preparation and examination

After the deposition, the beads and parts were prepared through standard metallurgical preparation including cutting, mounting, grinding, and polishing processes for the further metallurgical and mechanical analysis. The prepared cross section was etched with 2% Nital (98% ethanol and 2% HNO_3) for AM-XC-45 samples and Aqua Regia (HCl:HNO_3=3:1)＋Nital (98% ethanol and 2% HNO_3) for Stellite 6 samples. The optical microscopy (Keyence VHX-5000, Osaka, Japan) was used to observe the microstructure. For the mechanical testing, the tensile samples were prepared in the vertical and horizontal directions, as shown in Figure 3.5, according to ASTM E8M-09 standard and tested at room temperature according to the DIN EN 6892-1 standard by means of Instron-5550 tensile testing machine (Norwood, MA, USA).
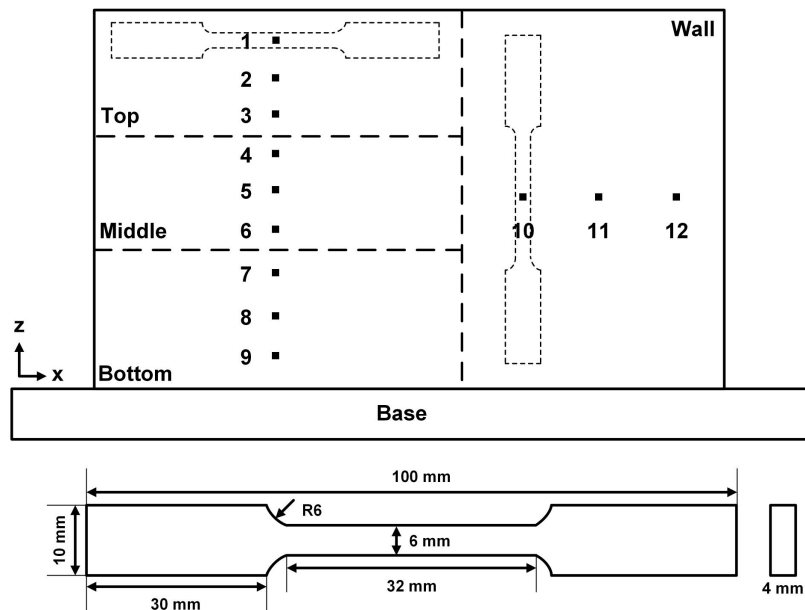
Figure 3.5 Schematic of the tensile test specimens extracted from the WAAM sample.

In addition, fractography was performed using a JEOL JSM-IT100 scanning electron microscope (SEM, Tokyo, Japan). Phase analysis and element distribution were measured using energy dispersive spectroscopy (EDS). High-resolution microstructural characterization was carried out using a JEOL FEG-SEM JSM 5600F scanning electron microscope (SEM) operated at 15 kV. Vickers hardness (HV_2, with 2 kgf, for AM-XC-45 and $HV_{0.2}$, with 0.2 kgf, for Stellite 6) was measured, using a Struers DuraScan-70 hardness tester

(Struers Inc, Westlake, USA). To further qualitatively evaluate the resulting microstructure of WAAM Stellite 6 on the steel substrates, X-Ray Diffraction (XRD) was performed. The Bruker D8 Advance diffractometer Bragg-Brentano geometry with graphite monochromator and Vantec position sensitive detector were used. Samples were scanned without spinning using Co K_α radiation (45 kV 35 mA) with a divergence slit 6A16 V20 and no scatter screen. The coupled θ-2θ scan performed using a 2θ step size of 0.035 º and counting time per step is 4 s. Similar phases were identified in both cases (Stellite 6+S355 and Stellite 6+AISI 420). The obtained X-Ray patterns were analyzed using the Bruker software DiffracSuite. EVA vs 5.0.

Bibliography

[1] Corus. European structural steel standard EN 10025-2:2004. Available online: https://www.tf.unikiel.de/matwis/amat/iss/kap_9/articles/en_steel_standards.pdf (accessed on 8 June 2019).

[2] Schneider, M., 1998. Laser cladding with powder, effect of some machining param eters on clad properties. Ph.D. thesis, University of Twente, Enschede, The Nether lands.

[3] Abbas, G., West, D., 1991. Laser surface cladding of stellite and stellite-SiC com posite depositsfor enhanced hardness and wear. Wear 143 (2), 353 – 363.

[4] Valsecchi B, Previtali B, Gariboldi E. Fibre laser cladding of turbine blade leading edges: the effect of specific energy on clad dilution[J]. International Journal of Structural Integrity, 2012, 3(4): 377-395.

[5] W. Ya, B. Pathiraj, S. Liu, 2D modelling of clad geometry and resulting thermal cycles during laser cladding, Journal of materials processing technology 230 (2016) 217-232.

[6] Ya, W.; Hernández-Sánchez, J.; Pathiraj, B.; Veld, A.H.i.t. A study on attenuation of a Nd: YAG laser power by co-axial and off-axial nozzle powder stream during cladding. In Proceedings of International Congress on Applications of Lasers & Electro-Optics, Miami, FL, USA, 6 October 2013; pp. 453–462.

[7] Ya W. Laser materials interactions during cladding: analyses on clad formation, thermal cycles, residual stress and defects[J]. 2015.

<p style="text-align: right; font-size: 2em;">4</p>

Investigation of Medium Carbon Steel Deposits Obtained Via WAAM using AM-XC-45 Metal-Cored Wire [1]

For the study of WAAM deposition using the AM-XC-45 metal-cored wire, a single bead wall containing ninety layers in total was deposited. Microstructure, hardness, tensile strength, and fractography of the deposited wall were investigated. The comparison of mechanical properties between WAAM and traditionally processed AM-XC-45, such as casting, forging, and cold rolling was provided in this chapter.

4.1 Macroscopic inspection

The single bead wall composed of ninety layers is shown in Figure 4.1. The final dimensions were measured to be around 190 mm in length, 160 mm in height, and 7 mm in width. As seen in Figure 4.2, the peak-to-valley variation (the distance between the highest and lowest point of the surface) on the top part of the wall was measured to be ~600 μm. The peak-to-valley variation could be caused by bead shape variation due to molten pool instability. It has been reported that higher heat input contributes to decreased surface waviness [1]. Therefore, with the wall building up, the heat input fluctuation in the molten pool caused by the change of heat dissipation condition results in molten pool instability, such as oscillation. In addition, because of the adequate cooling after each layer, the heat accumulation was controlled, so that no significant distortion was noticed for both the base and the wall.

Figure 4.1 The single bead wall using AM-XC-45 wire as deposited with WAAM.
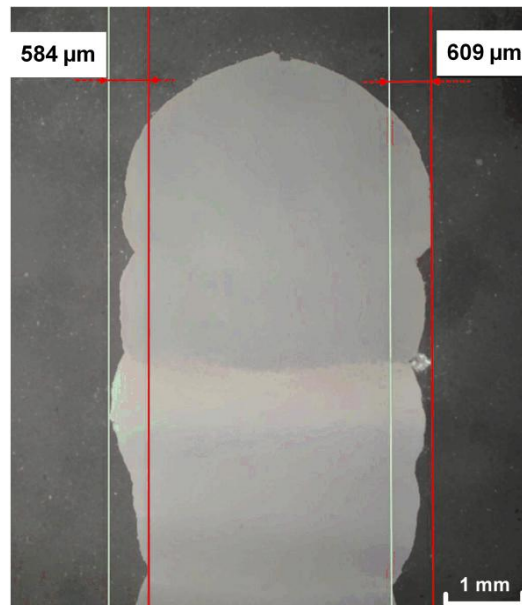
Figure 4.2 The local cross section at the top region of the wall.

4.2 Microstructure evolution during WAAM deposition

The microstructure was investigated at different locations within the WAAM deposited wall (as indicated in Figure 4.1). Representative etched cross sections at those locations are presented in Figure 4.3. The cross section revealed the ferrite (white), pearlite (black island), and bainite (black sheaf) phases.

Columnar grains were found at the top of the wall (region A). These columnar grains were directed perpendicular to the fusion line due to the preferential grain growth in the maximum thermal gradient. The prior austenite grains were decorated by grain boundary ferrite. The temperature was measured with a

thermocouple at the middle of the deposited track after each layer was deposited, from which the cooling rate was measured by thermocouple to be approximately 85.7 °C/s from 1100 °C to 800 °C and 28.5 °C/s from 800 °C to 500 °C.
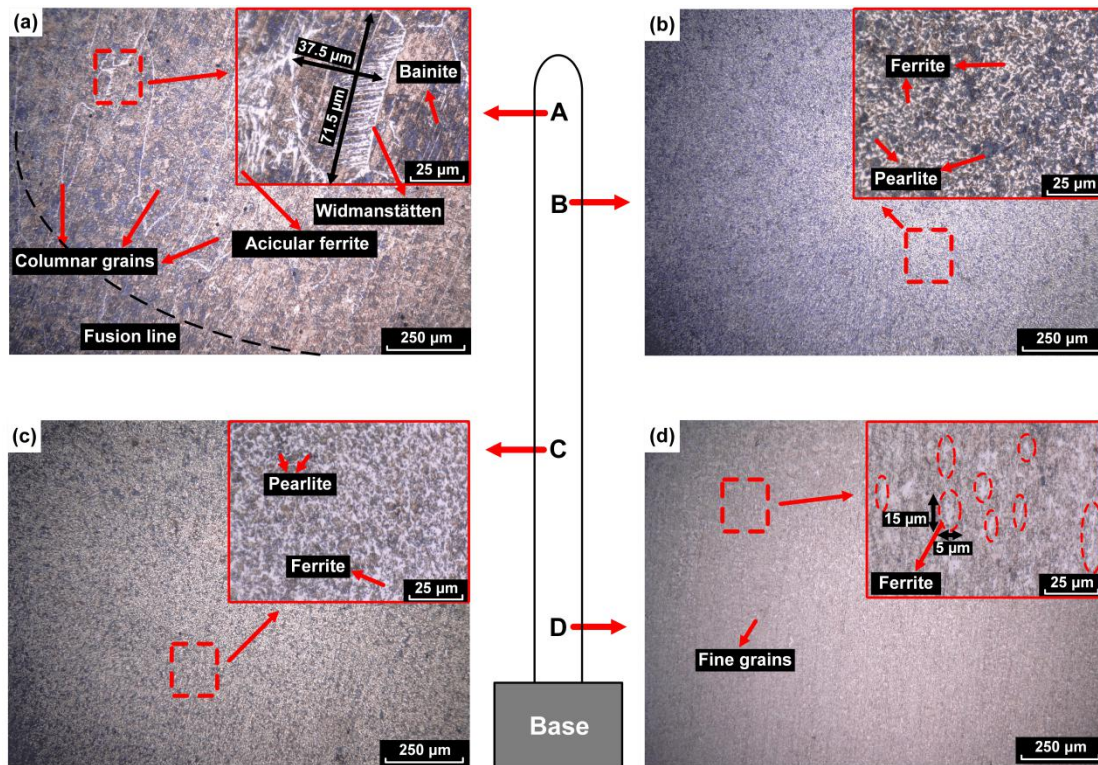
Figure 4.3 Microstructure of AM-XC-45 single bead wall at different locations, (a) region A; (b) region B; (c) region C; (d) region D.

The microstructures observed by optical microscopy in regions B and C are shown in Figure 4.3b and 4.3c, respectively. From the entire of the two micrographs, it can be seen that the microstructure included ferrite (white) and pearlite (black). The microstructure, in general, became finer from the top to the bottom of the wall.

To have a clearer characterization of the microstructure, a higher resolution micrograph was taken by SEM at region C, which is shown in Figure 4.4. Some carbide precipitates and oxide particles (black spots in Figure 4.4a) were found in this region. The pearlite lamellae are shown in Figure 4.4b and the carbide precipitates are dispersed within the ferrite, as shown in Figure 4.4c. As seen in Figure 4.4b, the pearlite lamellae appeared to have thickened and contained edges. This was an indication that during reheating, the pearlite transformed into high carbon austenite, which then transformed to martensite during cooling. This was possible because of the high local hardenability of the carbon enriched austenite. The finest grains were observed in region D, as shown in Figure 4.4d. The grain size reduction was a result of the multiple thermal cycles experienced by the material. After the multiple thermal cycles, the ferrite and pearlite became finer. This can be proved by the measured maximum width and length of the prior austenite grains in region A and region D. The maximum width/length of the grain decreased from 37.5 μm/71.5 μm in region A to 5 μm/15

24

µm in region D. It can also be seen that the nucleation of ferrite occurred preferentially at prior columnar austenite grain boundaries.
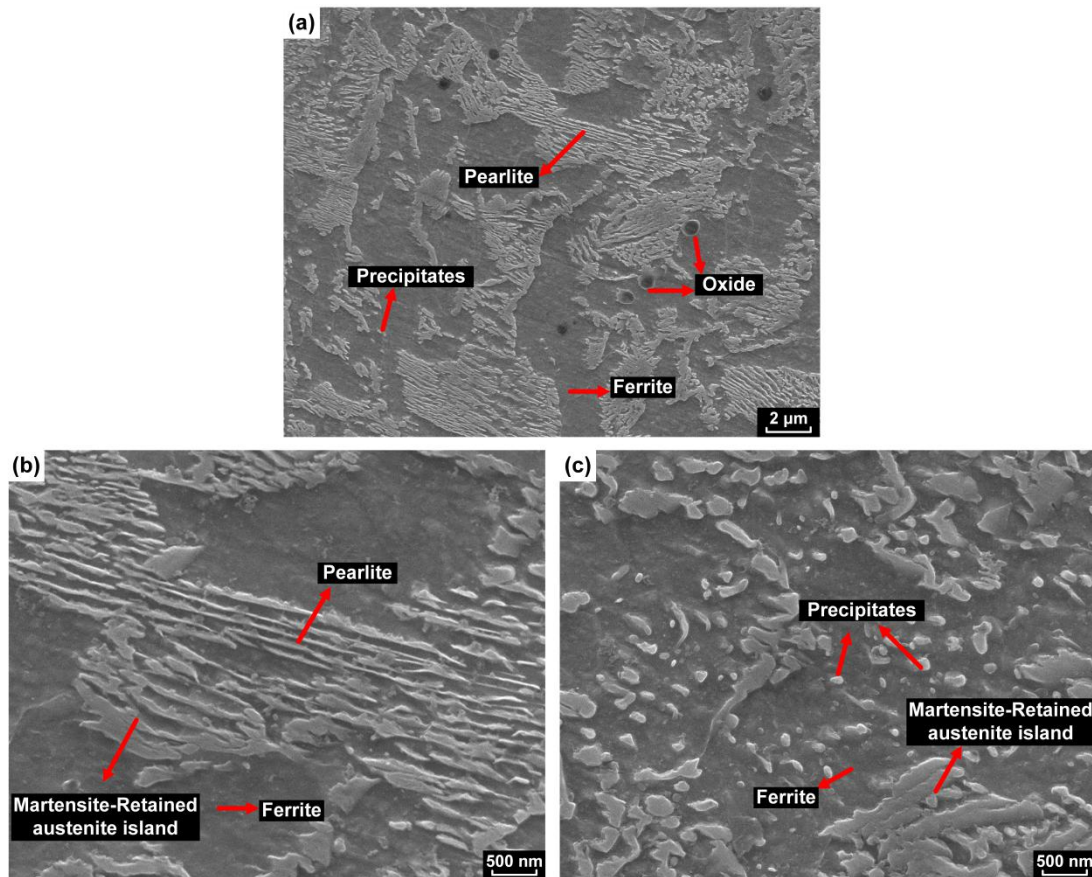
Figure 4.4 High-resolution micrograph of region C, (a) low magnification; (b) high magnification of pearlite; (c) high magnification of precipitates.

4.3 Hardness of the WAAM deposited wall

The variation of hardness along the vertical direction of the deposited wall is plotted in Figure 4.5a. In general, the deposited material undergoes several thermal cycles, which is expected to affect the hardness [2,3]. In the present case, the average measured hardness of bottom, middle, and top regions were 238 ± 8 HV, 243 ± 5 HV, and 250 ± 4 HV, respectively. The hardness of the top layers was slightly higher than the bottom layers because of the presence of non-equilibrium phases such as bainite and Widmanstätten ferrite, as seen in Figure 4.3a. The measured hardness (Figure 4.5a) showed that the fluctuation of hardness in the middle region was the smallest, while that of the top and bottom regions was larger. This indicated that the mechanical properties within the middle region were suspected to be more uniform.

A combination of microstructural factors affects hardness values. In the present case, the hardness depended on the local phase constituents, the grain size, and the fraction and size of the precipitates. The phases present could exhibit a hardness variation due to their exposure to high temperatures. High-temperature

exposure induced tempering, recovery, and recrystallization effects, which decreased the hardness, while at the same time, precipitation of carbides and martensitic transformation contributed to a hardness increase. These effects were different along the build direction, as it was largely dependent on the cooling rate and the number of subsequent heat cycles that each layer was exposed to. Therefore, three different zones were distinguished:

a) The lower part of the wall, region D. In this region the cooling rate was influenced by the base. The lower regions experienced the highest number of re-heating cycles due to the subsequent layers. Additionally, the composition of the first layers varied slightly, as the dilution of the consumable with the base took place. All these factors were expected to contribute to a lower hardness value and possibly higher elongation in the tensile test.

b) The middle part of the wall, regions C and B. In these regions, cooling, apart from convection and radiation, which was similar for all layers, was governed by conduction through the already deposited layers. Therefore, the cooling rate of this region was lower than that of the region D, resulting in a relatively homogeneous hardness. The middle part of the wall also experienced re-heatings, therefore tempering effects also contributed to the mechanical property values. Tempering effects were pronounced in the middle region because there was no influence of the base plate during cooling.

c) The top part of the wall, region A. This was the last deposited section of the wall, in which the cooling rate was as in the previous case b), but the number of re-heating cycles experienced to induce significant tempering effects was reduced. Therefore, this region was likely to exhibit higher hardness values.
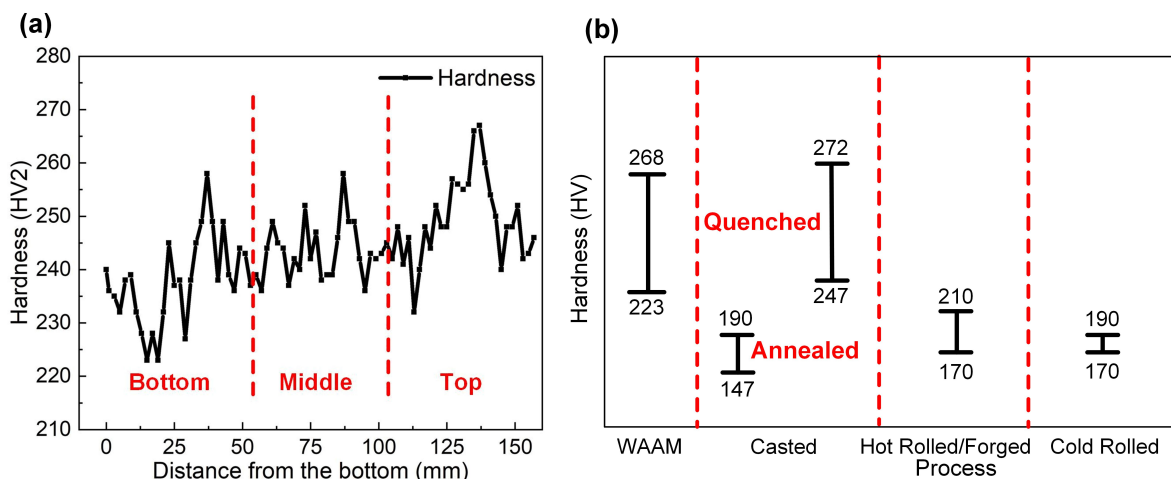
Figure 4.5 (a) Hardness of the AM-XC-45 wall from the bottom to the top; (b) Hardness comparison of different processes.

The hardness of the WAAM deposited wall was compared with the hardness of AM-XC-45 from different manufacturing processes, as shown in Figure 4.5b. It shows that the WAAM deposited AM-XC-45 metal-cored wire had a comparable hardness with the other processes.

4.4 Tensile strength evaluation of the WAAM deposited wall

The measured yield and tensile strength together with the elongation of the samples prepared in different directions are summarized in Figure 4.6. The measurements showed that there was anisotropy in mechanical behavior within the WAAM deposited wall. The tests showed that both yield and ultimate strength decreased from the top to bottom layers. This was in agreement with the hardness profile shown in Figure 4.5a.
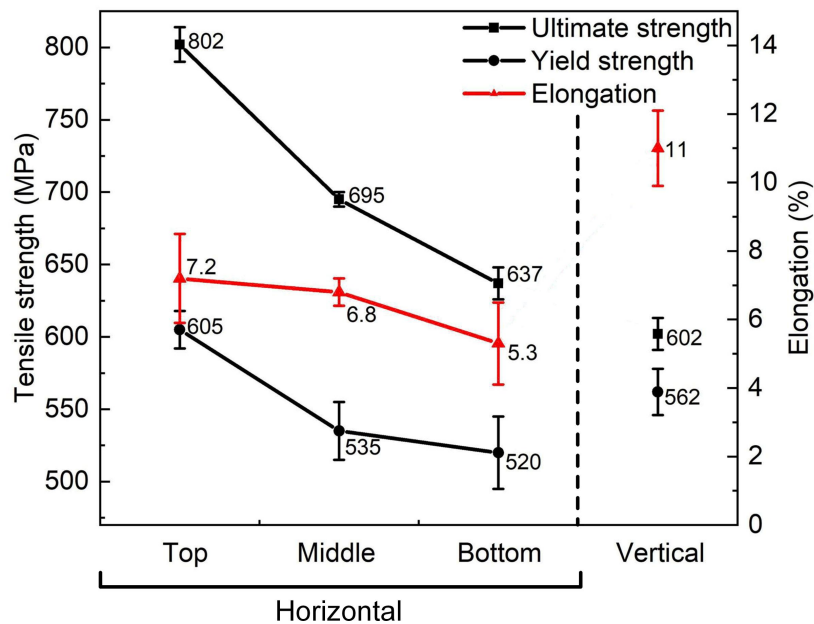
Figure 4.6 The measured yield strength, ultimate strength, and elongation.

It also can be seen that there was an apparent elongation difference between the horizontal and vertical direction. The existence of ferrite grains nucleated at columnar prior austenite grain boundaries contributed differently to the strength and elongation in the horizontal (deposition) and vertical (build) direction [4]. The anisotropic nature of additive manufactured material properties was also reported by other researchers [5,6].

These average values of the WAAM deposited with AM-XC-45 metal-cored wires were compared with the results of traditional metal processing (based on AISI 1045 steel) methods, which is shown in Figure 4.7. The yield strength and ultimate strength produced by WAAM were higher than most of the conventional manufacturing methods, while the elongation was lower. This corresponded well with the hardness results presented in Figure 4.5, which also shows that the average hardness in the quenched condition was higher than for the other techniques. In order to improve the ductility of the AM-XC-45 WAAM deposited material, we considered additional post-deposition heat treatments to acquire the desired ductility. The possible heat treatments for AM-XC-45 WAAM is a topic that was not covered in the current study.
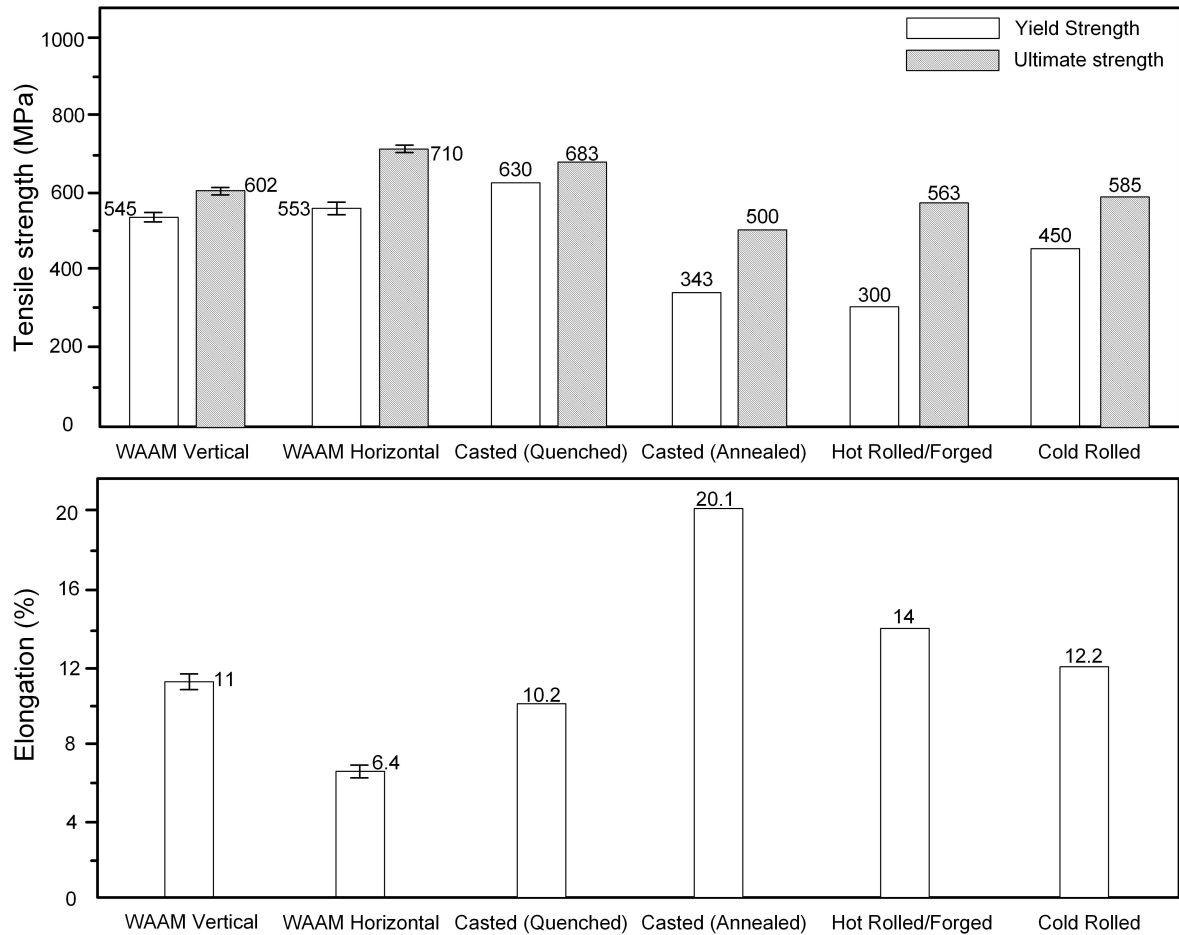
Figure 4.7 Tensile strength comparison of different process.

4.5 Fractography

According to the results of tensile test, the samples 3, 6, 8, and 11 (shown in Figure 3.3) were the samples from the top, middle, bottom, and vertical positions, respectively. Therefore, the fracture surfaces of these tensile samples (number 3, 6, 8, and 11) were observed by means of SEM, as shown in Figure 4.8. All examined tensile samples showed a non-porous ductile fracture, which was reflected by the dominance of dimples in all fracture surfaces, as seen in Figure 4.8a. Inclusions were also observed inside dimples. These sites had a higher possibility to nucleate cracks.
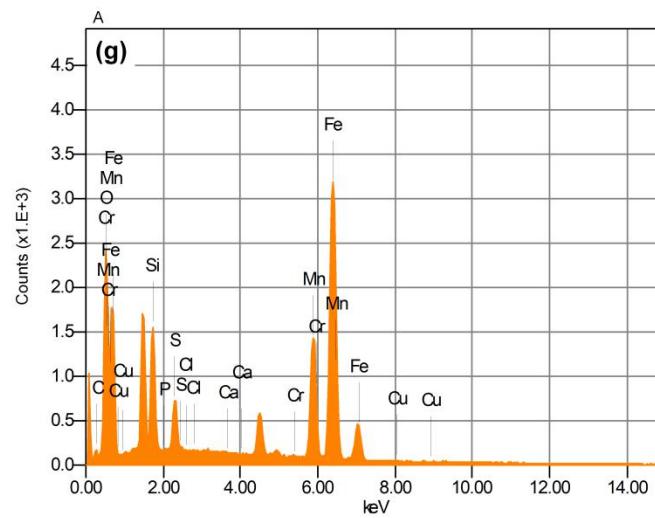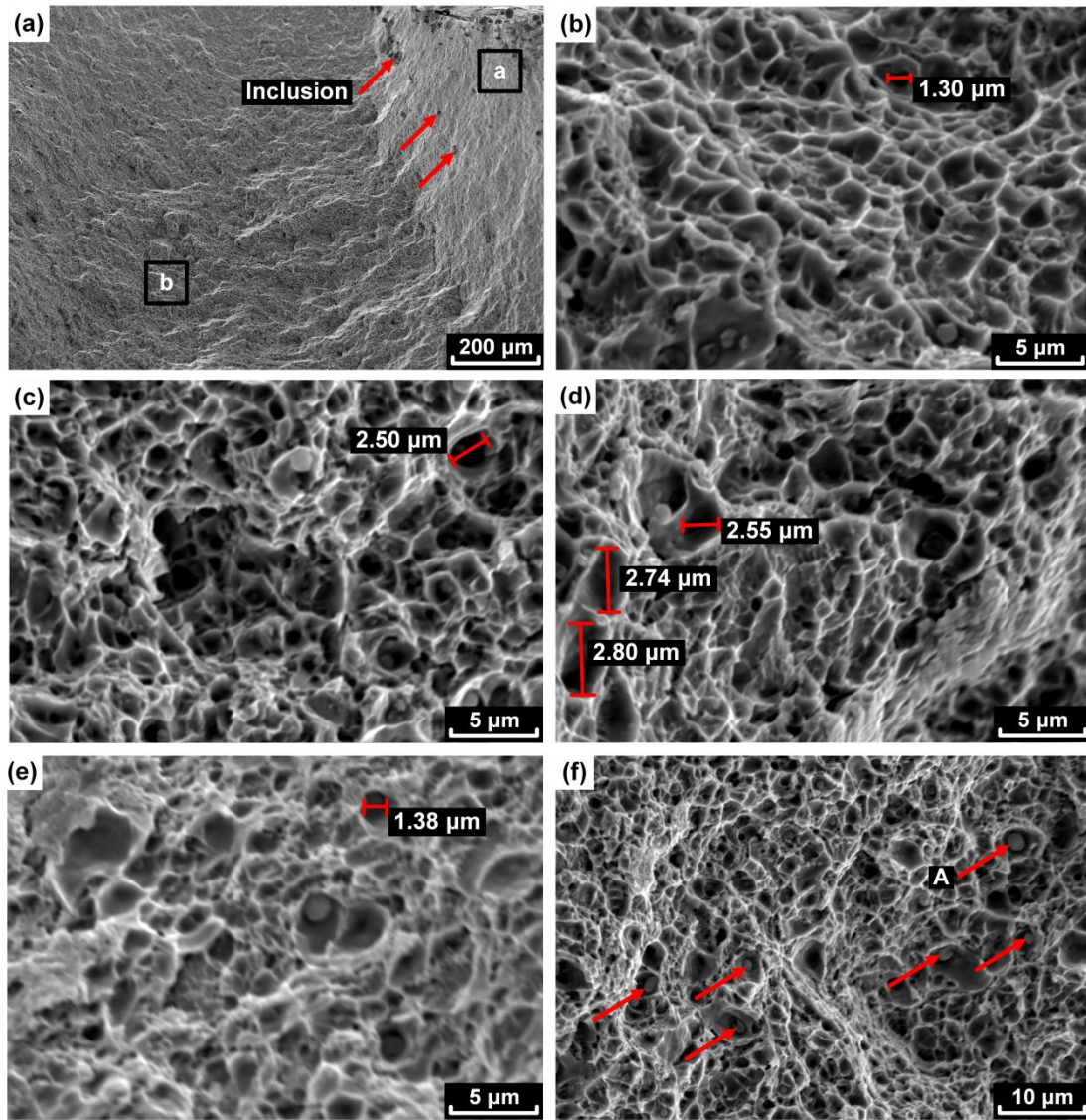
Figure 4.8 Fractography of tensile samples, (a) Low magnification; (b) Bottom; (c) Middle; (d) Top; (e) Vertical; (f) EDX particles; (g) EDS plot of particle A.

Comparing Figure 4.8b–4.8e, the dimple size in the horizontal samples (numbers 3, 6, and 8) were found to be similar to that in the vertical sample (number 11). Due to the micro-void coalescence effect [7], some large dimples appeared locally.

The particle (A) could be found inside the dimples. The existence of the metallic phases or oxides could promote the formation of dimples. Smaller dimples were probably related to the voids initiating at grain boundaries or other microstructural features. Larger dimples tended to nucleate at oxide particles [8]. Energy-dispersive spectroscopy (EDS) analyses were performed at particle A (Figure 4.8f) and the results are shown in Figure 4.8g. It can be seen that O, Fe, Mn, Cr, Si, and S were the main elements in particle A, which could be identified as either non-metallic inclusion, such as MnS [9] or oxide.

4.6 Conclusions

The microstructure and mechanical properties of WAAM material deposited with AM-XC-45 metal-cored wires were investigated. Despite the challenging material composition, due to the high carbon content, the deposited wall showed good structural integrity and as-deposited mechanical properties attractive for industrial application. From the study, the following conclusions can be drawn:

a) The mechanical properties comparison between WAAM produced AM-XC-45 part and AISI 1045 part produced by traditional processes was carried out. The hardness and tensile strength with WAAM are larger or comparable with the values from the quenched condition.

b) The variation of hardness from bottom to the top of the wall is in the range between 223 HV and 268 HV.

c) The tensile strength difference exhibits anisotropy between build direction and the horizontal direction, which is around 200 MPa. The mean vertical elongation of the WAAM produced AM-XC-45 wall is 11%, which is higher than 6.4% in the horizontal direction.

d) The fracture of the WAAM produced AM-XC-45 wall is ductile. Some particles existing as inclusion, such as MnS or oxide, are found on the fracture surface.

e) Pearlite, ferrite, bainite, and martensite are present in the constructed wall. Columnar grains are found near the fusion line. In addition, the repeated thermal cycles cause the grains to become finer from the top to bottom layers.

Based on the results found in this study, it has great potential to apply metal-cored wires in WAAM applications.

Bibliography

[1] Rodrigues T A, Duarte V, Avila J A, et al. Wire and arc additive manufacturing of HSLA steel: Effect of thermal cycles on microstructure and mechanical properties[J]. Additive Manufacturing, 2019, 27: 440-450.

[2] Wang T, Zhang Y, Wu Z, et al. Microstructure and properties of die steel fabricated by WAAM using H13 wire[J]. Vacuum, 2018, 149: 185-189.

[3] Haden C V, Zeng G, Carter III F M, et al. Wire and arc additive manufactured steel: Tensile and wear properties[J]. Additive Manufacturing, 2017, 16: 115-123.

[4] Ling-kang J, Yang L, Li M, et al. Analysis of Microstructure and Orientation in X80 Line Pipe Steels[J]. 2011.

[5] Carroll B E, Palmer T A, Beese A M. Anisotropic tensile behavior of Ti–6Al–4V components fabricated with directed energy deposition additive manufacturing[J]. Acta Materialia, 2015, 87: 309-320.

[6] Casati R, Lemke J, Vedani M. Microstructure and fracture behavior of 316L austenitic stainless steel produced by selective laser melting[J]. Journal of Materials Science & Technology, 2016, 32(8): 738-744.

[7] Pradhan P K, Robi P S, Roy S K. Micro void coalescence of ductile fracture in mild steel during tensile straining[J]. Frattura ed Integrità Strutturale, 2012, 6(19).

[8] Das A, Tarafder S. Geometry of dimples and its correlation with mechanical properties in austenitic stainless steel[J]. Scripta Materialia, 2008, 59(9): 1014-1017.

[9] He J, Lian J, Golisch G, et al. Investigation on micromechanism and stress state effects on cleavage fracture of ferritic-pearlitic steel at− 196 C[J]. Materials Science and Engineering: A, 2017, 686: 134-141.

Investigation of Stellite 6 Deposits on Steel Substrates Obtained Via WAAM using Metal-Cored Wire [2]

In the direct energy deposition (DED) process, it is essential to understand how the material responses to the supplied heat during the additive manufacturing (AM) process. The responses in our case include the bead geometry, dilution, microstructure, and microhardness, which can help to determine the optimal deposition conditions. The effect of different heat input levels (combinations of different deposition parameters) on the bead characteristic can be obtained through the ramping tests.

5.1 The bead geometry and process window

The Figure 5.1 shows the Stellite 6 bead deposited at various conditions using the ramping technique. The discontinuous and unstable beads, appearing due to the low heat input, was marked with a yellow dash line. As the heat input increases, it is easier to deposit continuous beads. The energy is sufficient to melt the electrode filler metal and encourage the spreading of the melt, because the surface tension is reduced. The continuously deposited beads were marked with the blue dash line in Figure 5.1. However, the narrow bead shape resulted in a small aspect ratio. More energy is required to obtain a better bead shape suitable for overlapped deposition. The further increasing heat input facilitates the molten pool spreading, which results in wider bead, hence a lager aspect ratio. Samples shown in Figure 5.1 were subsequently cut and cross sections were prepared for further analysis.

---

[2] This chapter is based on the article: Z. Lin, W. Ya, C. Goulas, B. A. di Castri, V. Venkata Subramanian, M.J.M Hermans, Depositing of Stellite 6 alloy on steel substrates using Wire and Arc Additive Manufacturing, to be submitted to Journal of Materials Processing Technology.
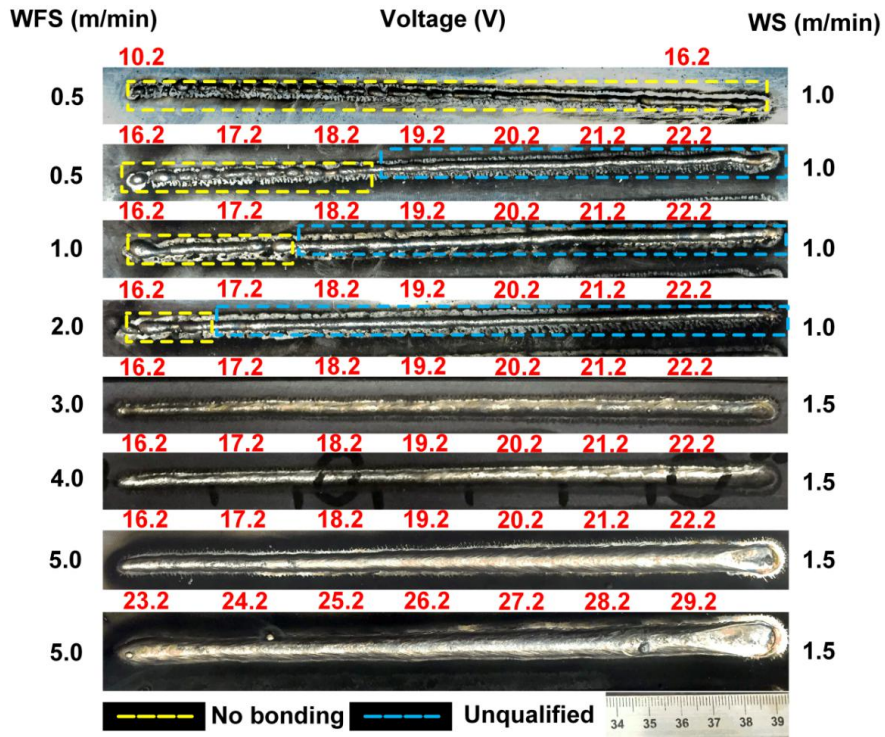
Figure 5.1 The overview of the ramped deposits.

A process window is generated based on the cross sections obtained from Figure 5.1 as shown in Figure 5.2. The minimum heat input to obtain a qualitative bead during WAAM depositing Stellite 6 was found to be around 55 J/mm in our study. The aspect ratio varies from 2.25 to 4 at different heat input levels. Dilution below 5% can be achieved, which is equivalent to laser deposition [1]. As heat input increased, both aspect ratio and dilution increases. It is beneficial to have a larger aspect ratio, which is helpful to avoid the unfilled caused by the overlapped bead near the weld toe and obtain a good metallic bonding between base and deposit as well [2,3]. When the wire feeding is constant, a bead shape with a larger width and smaller height can be deposited. Furthermore, heat input needs to be controlled to limit the distortion of the substrate and avoid excessive dilution [4]. If dilution is excessive, it can compromise the material properties of the deposit and reduce the wear or corrosion performance of the deposited layer. Therefore, bead geometry, dilution, and hardness need to be considered during parametric optimization, where the lower dilution will have a minimum influence on the deposited material properties, a larger aspect ratio will be preferable for overlapped deposition, and desirable hardness value to provide sufficient material properties.

Schneider [5] has reported that 15% of the dilution for laser depositing Stellite 6 on steel substrate is to be effective in achieving clad layers with good hardness and bonding. It was also reported that the hardness can reduce to around 500 $HV_{0.2}$ [6] when the dilution is above 28%. According to the data shown in Figure 5.2, to ensure the material properties with good bead geometry, the dilution level can be kept between 10% and 20%, which can be used as primary criteria for the process optimization. Therefore, the conditions A, B, C, D and E as shown in Figure 5.2, were identified as candidates for further study in the overlapped deposition experiments. As the dilution levels of B, C and D are similar, only condition D was selected as it has a

relative larger aspect ratio. For comparison, the conditions A and E were also studied as they can be representative at different dilution levels. Hence, microhardness measurements were performed on the single beads deposited using conditions A, D and E on S355 steel substrate. The average hardness measured was 581 ± 16 $HV_{0.2}$ (condition A), 553 ± 11 $HV_{0.2}$ (condition D) and 506 ± 10 $HV_{0.2}$ (condition E).
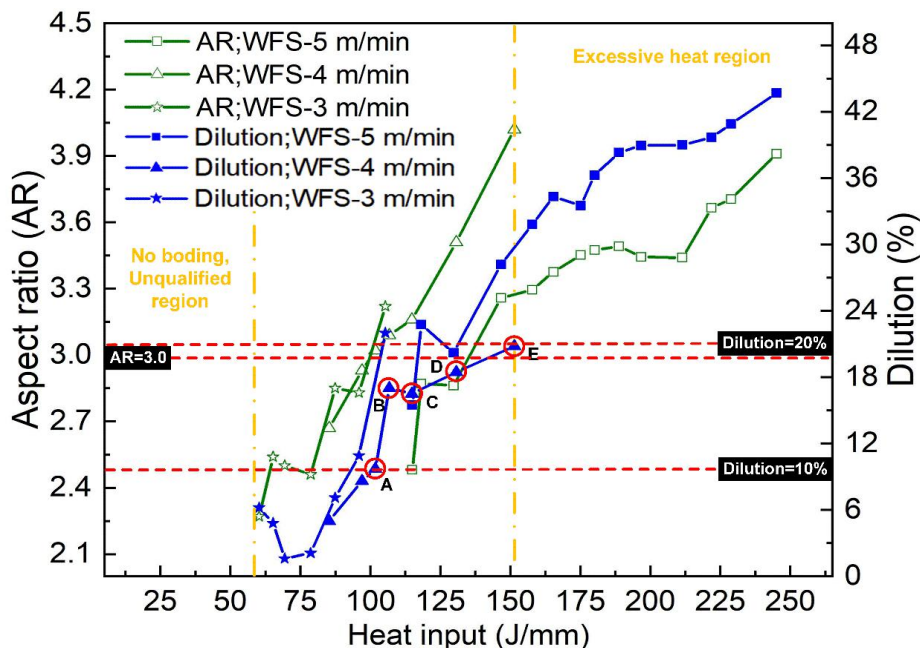
Figure 5.2 The WAAM process window for Stellite 6 deposition.

5.2 Microstructure of Stellite 6 deposited on steel substrates

Figure 5.3a is the cross section of the WAAM deposited Stellite 6 on the S355 steel substrate, which includes different microstructural features in the substrate, at the fusion line, and within the deposit. The resulting microstructure at different locations (Figure 5.3a-5.3f) of the bead was examined using optical microscopy (OM). In addition, the microstructure in the HAZ is better revealed under scanning electron microscopy as shown in Figure 5.3f. Ferrite and martensite (Figure 5.3f) are found below the fusion line on the substrate side. The complex microstructure was not expected.
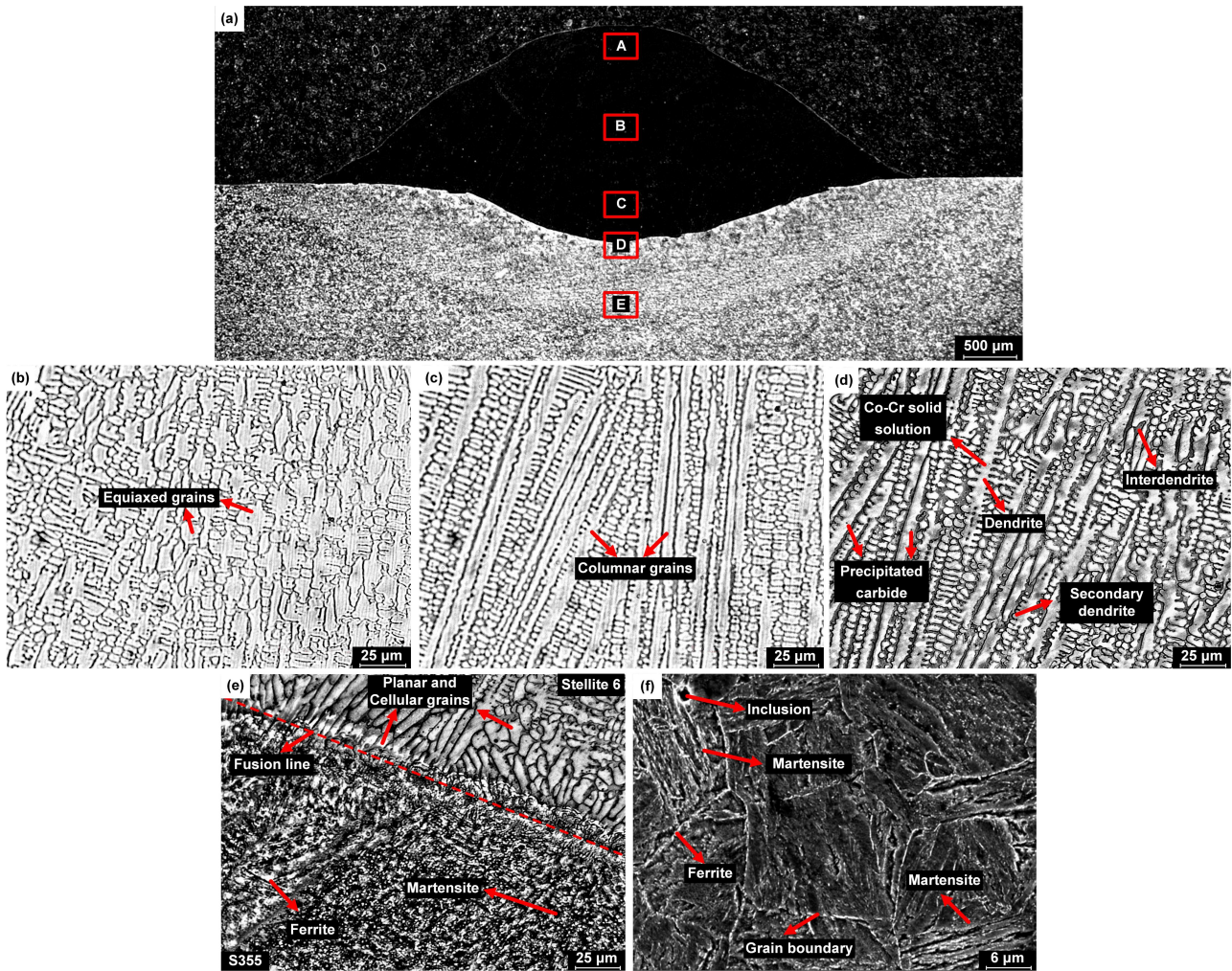
Figure 5.3 Cross section of Stellite deposits on the S355 using condition D, (a) overview; (b) top of the bead (location A); (c) centre of the bead (location B); (d) within the bead close to fusion line (location C); (e) around the fusion line (location D); (f) in the substrate (location E).

The variation of the microstructural morphology from the fusion line towards the top of the beads indicated that the cooling rate (and temperature gradients (G)) at different locations during solidification varies. From the fusion line to the center of the bead, the solidification speed increases and the temperature gradient decreases. Planar grain growth (Figure 5.3e) observed at the fusion line where the nucleation initiated at the start of the solidification. This is due to the ratio of the temperature gradient (G) over the interface (solid-liquid) moving velocity (R) is much larger at the fusion line than other positions of the molten pool [7]. It follows the cellular (Figure 5.3e) and columnar grain growth towards the centre of the bead where the primary grain solidifies following the maximum cool direction (Figure 5.3c and 5.3d). Small equiaxed grains were observed around the bead where the conduction cooling with ambient occurs which restrain the fast grain growth. This results in finer grain as its cooling rate is relatively higher than the centre of the bead.

In general, the observed microstructures in the Stellite 6 deposits belong to a hypoeutectic structure including the primary dendritic cobalt solid solution and the eutectic of a mixture with Co-Cr solid solution

and Cr-rich carbides. These carbides can strengthen the cobalt matrix and increase the hardness in the solid solution. During the solidification process, the light phase (OM) formed as primarily the dendrites is expected to be a Co-rich solid solution (γ phase), Co-Cr solid solution with FCC crystal structure initially appeared as matrix [8].
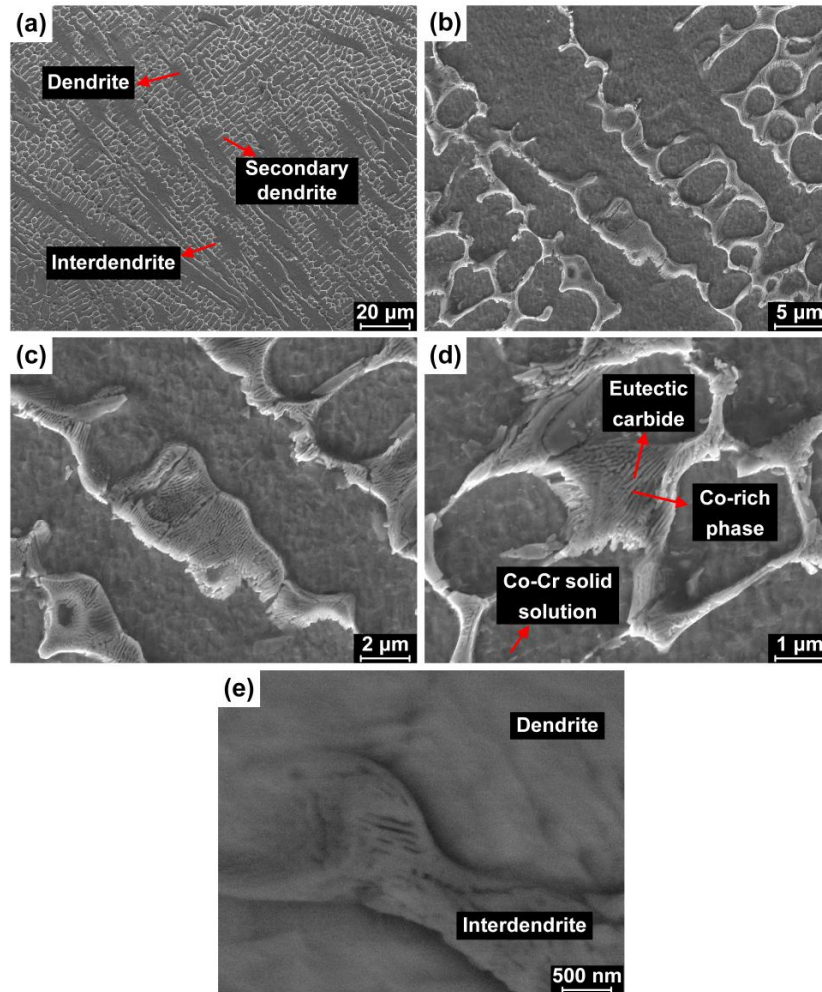
Figure 5.4 SEM micrograph of WAAM deposited Stellite 6, (a) overview of Stellite 6 deposits; (b) primary and secondary dendrites; (c) lamellar interdendrite and dendrite; (d) eutectic carbide; (e) Dendrite and interdendrite morphology at high resolution.

The precipitated carbides (black dot) are found within the matrix, and the carbides are also expected to appear in the interdendritic eutectics observed the dark region (OM). These fine carbides can provide dispersion strengthening [9] and contribute to both the strength and the wear resistance. The high-resolution SEM micrograph of WAAM deposited Stellite 6 is shown in Figure 5.4a-5.4d. The lamellar interdendrite is composed of Co-rich solid solution and eutectic carbides as indicated in Figure 5.4d. The eutectic carbides existing as a network formed inside the interdendrite and mixed with Co-rich phase (Figure 5.4e). The dendritic region is expected to be richer in Co and the interdendritic region is expected to be richer in Cr, W, C and Si elements. Cr, W, C and Si elements in the interdendritic regions can contribute to the formation of hard carbides such as $Cr_{23}C_6$ and Cr_7C_3 [10].

Similar analyses were performed on the samples produced using conditions A and E, which the microstructure behaviors from the fusion line to the top of the deposited bead were comparable as condition D (as shown in Figure 5.3). The most significant difference (as shown in Figure 5.5) was that the grain size increased with the increase of heat input, which has also been observed and reported by other researchers [11,12]. The size of the primary solidified dendrites increases with increased heat input, indicating that the cooling rate becomes smaller. This can contribute to a hardness reduction together with the Fe dilution from the substrate, which has also been reported in the literature [13,14].
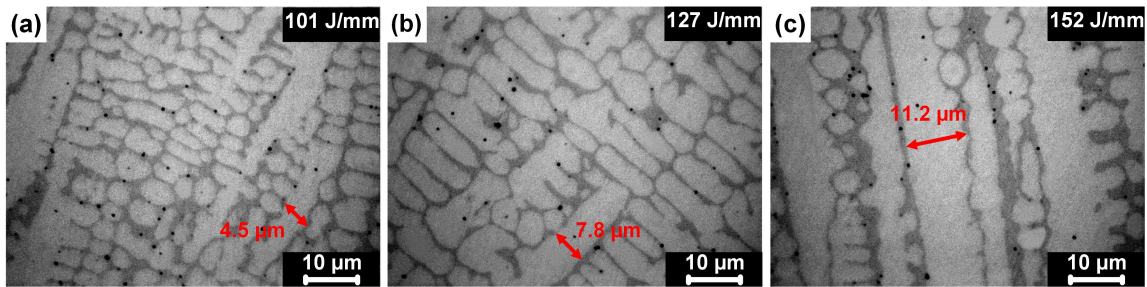
Figure 5.5 The grain size under different heat input, (a) Parameter A; (b) Parameter D; (c) Parameter E.
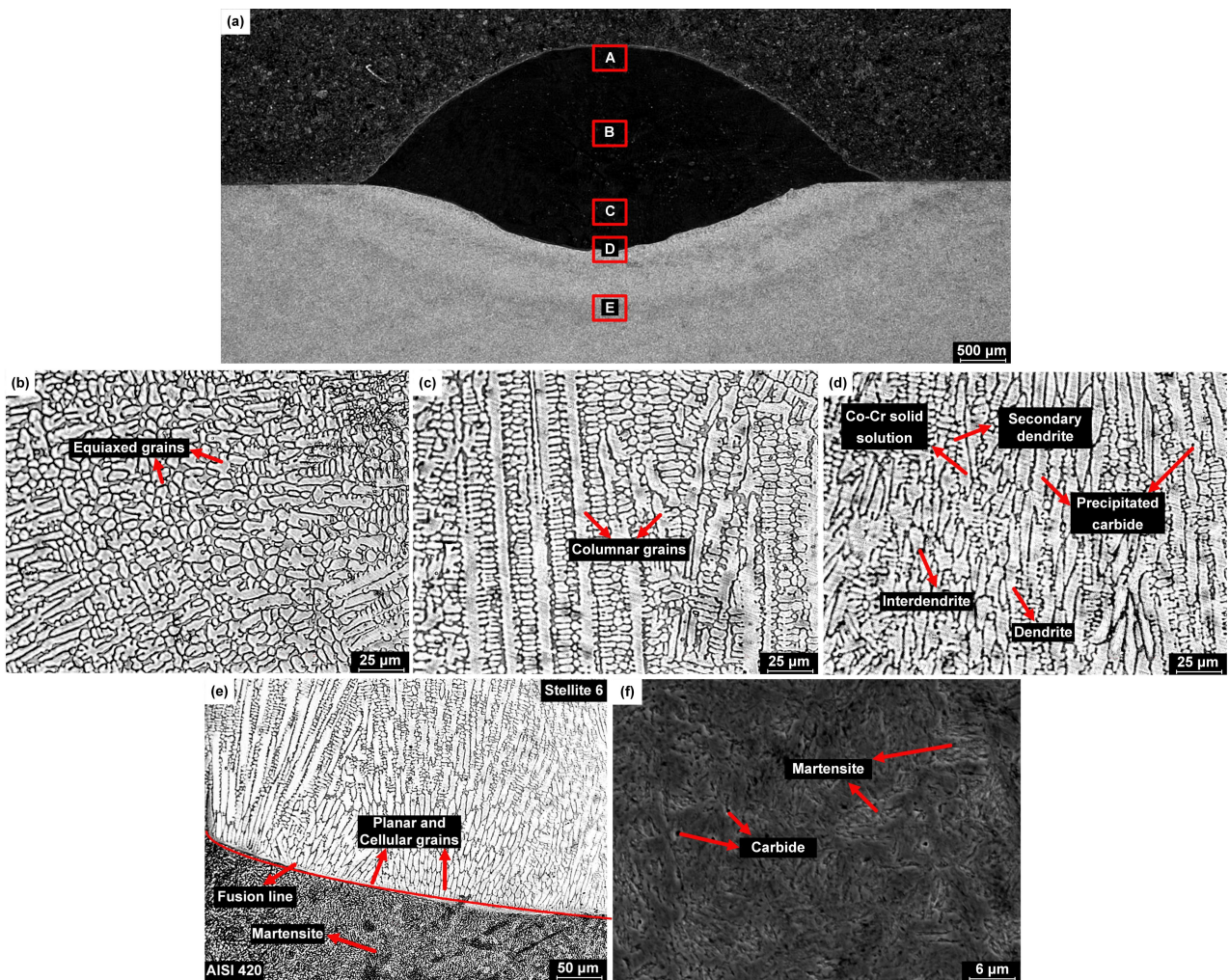
Figure 5.6. Cross section of Stellite 6 deposits on the AISI 420 steel substrate using condition D, (a) overview; (b) top of the bead (location A); (c) centre of the bead (location B); (d) within the bead close to fusion line (location C); (e) around the fusion line (location D); (f) in the substrate (location E).

For comparison, Figure 5.6a is presented as the cross section of the WAAM deposited Stellite 6 on the AISI 420 steel substrate using the condition D. From the fusion line to the top of the deposit (Figure 5.6b-5.6f), similar microstructure behavior during solidification were observed as shown in Figure 5.3. Hence, it is expected that similar material properties to be obtained when condition D is used to WAAM depositing Stellite 6 on S355 and AISI 420 steel substrates.

5.3 Elemental distribution and dilution

Apart from the microstructure, the elemental distribution of the sample produced at condition A, D, and E on S355 steel substrate and the sample produced on AISI 420 stainless steel substrate were examined through the line scanning along the centre of the bead from the substrate to the deposits using Energy Dispersive Spectroscopy (EDS). The measurements are presented in Figure 5.7. It shows that the melt depth (distance between the fusion line and the substrate surface indicated) increases as increased heat input as observed and presented in Figure 5.2. When WAAM depositing Stellite 6 on S355 steel, the Fe dilution from the substrate is observed (Figure 5.7a-5.7c), which can lead to the hardness reduction [6]. The increase in the Fe content is suspected to be the reason for the hardness reduction as Fe promotes Co phase transition from HCP to FCC [15]. The experimental results obtained by Xu et al. [16] show that a Fe dilution of 46 % reduces the hardness to around 400 HV.
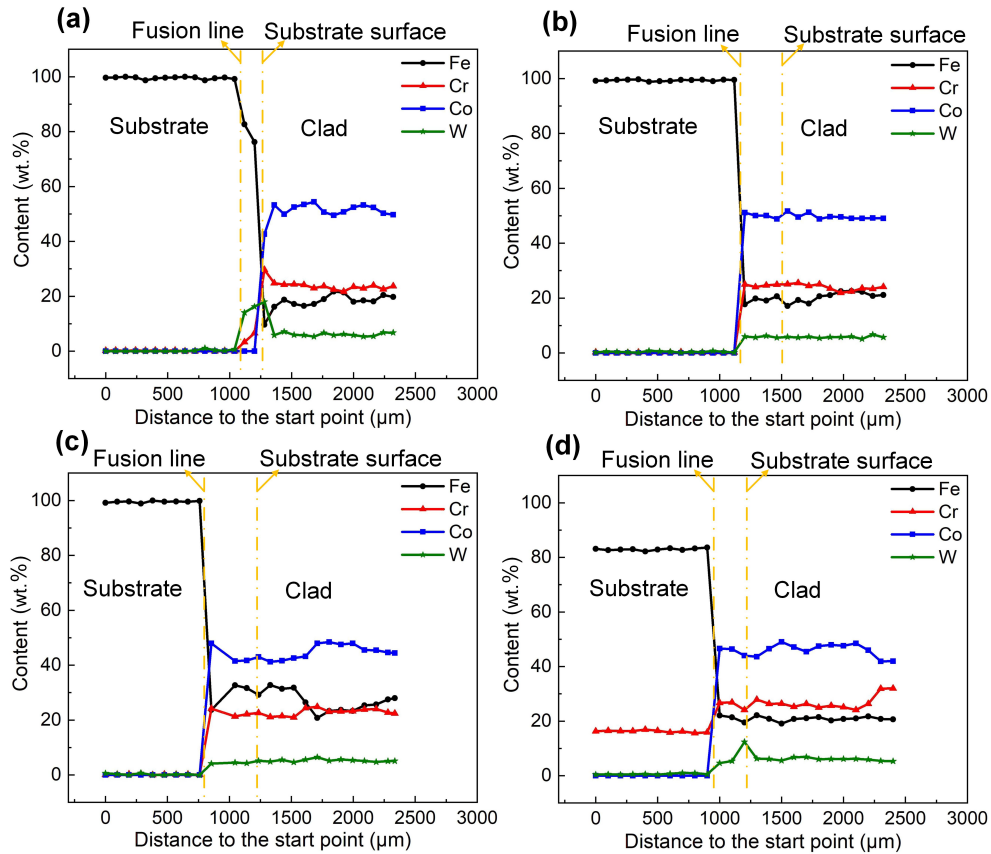
Figure 5.7 Elemental distribution measured using EDS, (a) condition A (Stellite 6+S355); (b) condition D (Stellite 6+S355); (c) condition E (Stellite 6 + S355); (d) condition D (Stellite 6 + AISI 420).

It is interesting noticed that the around 20% of Fe dilution in the deposits produced using condition A and ununiform Fe dilution in the deposit produced using condition D. In the first case, there is around 10% dilution was observed near the fusion line and stable around 20% within the deposit (Figure 5.7a). Around 30% dilution was observed in the deposit on the half near the substrate and around 20% dilution observed in the rest of the deposit (Figure 5.7c). This is contradicting with the dilution values calculated using the geometrical definition and presented in Figure 5.2. It was reported in the literature [17] that geometrical dilution can be used to represent the chemical dilution. For instance, more Fe atoms will diffuse from base side to Stellite 6 side for a deposit with higher geometrical dilution. However, the special case, such as observed in our study, the geometrical dilution fails to represent the chemical dilution. This was maybe introduced by the non-uniform molten pool flow during WAAM or other metallurgical reasons, which requires more detailed research and it is beyond the scope of this study.

It is observed that around 20% of Fe dilution within the deposits produced using condition D for both S355 and AISI 420 steel substrate. However, the melt depth in WAAM Stellite 6 on AISI 420 steel substrate is less than the WAAM Stellite 6 on the S355 steel substrate. Considering the thermal conductivity of the two materials, the opposite trend would be expected, as the thermal conductivity of the AISI 420 steel (23-27 [W m^{-1} K^{-1}]) is smaller than the S355 (32 [W m^{-1} K^{-1}]). However, lower melting depth is observed in WAAM

Stellite 6 on AISI 420 steel substrate samples. This could be explained by the fact that the supplied energy could partially contribute to the latent heat of martensitic transformation. This leads to a lower dilution and it is beneficial for preserving the properties of the deposits.

5.4 WAAM depositing overlapped beads - single layer

In practice, a surface is deposited by overlapping several beads (the so-called deposited layer), which can be scaled up for applications. Hence, several overlap ratio values (30%-60%) were investigated using conditions A, D, and E on both S355 steel substrates. The deposited layers under different conditions are presented in Figure 5.8a-5.8c. Based on the surface waviness (peak-to-valley distance of surface), dilution level (geometrical), and the elemental distribution, the 42% overlap ratio with condition D on S355 steel (Figure 5.8c) were identified to be optimal, when considering the balance between waviness and satisfactory dilution. These mentioned results are summarized in Table 5.1.

Therefore, both Stellite 6 single bead and overlapped beads were deposited on the AISI 420 steel substrates using condition D. The average hardness of the obtained single bead was measured to be 547 $HV_{0.2} \pm 7$ $HV_{0.2}$. The obtained waviness and dilution were comparable to the results of WAAM deposited Stellite 6 on S355 steel substrate (Table 5.1).
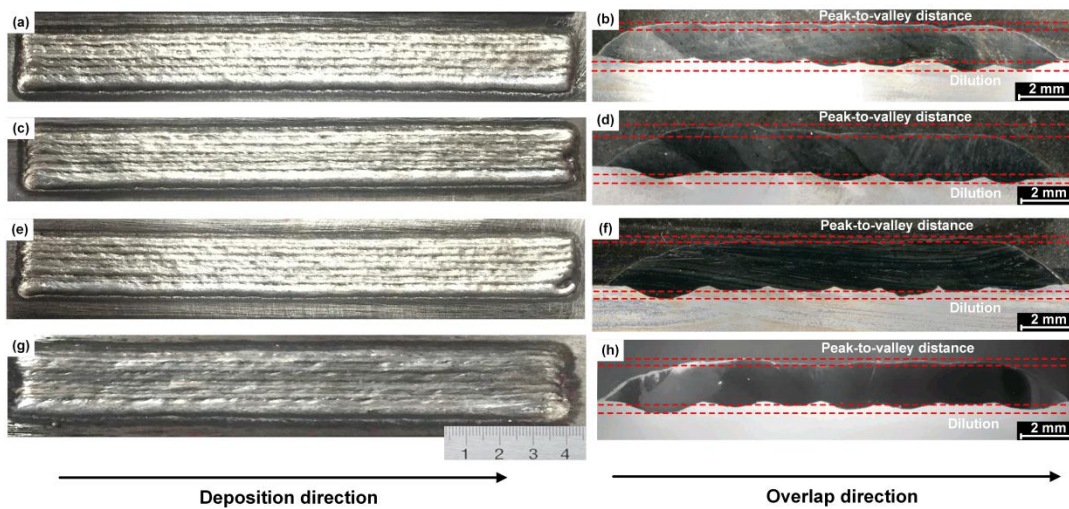
Figure 5.8 The macroscopic appearance and cross section morphology of deposited layer, (a), (b) condition A, S355; (c), (d) condition D, S355; (e), (f) condition E, S355; (g), (h) condition D, AISI 420.

It is interesting to observe from Figure 5.3 that with the increased heat input, the surface waviness reduced due to the molten metal can provide sufficient energy to support its flow. With the heat accumulation in the substrate, the dilution was expected to increase as deposition progressing and becomes stable eventually when a thermal balance is reached [18]. However, during WAAM overlapped bead deposition, the supplied arc energy was partially used to melt previously laid layer, resulting in less dilution as shown in Figure 5.3b

(d) (f) (h). It is important that the dilution can be kept at a satisfactory level (smaller than 28% as mentioned earlier) to maintain the material properties. The geometrical dilution level shown in Table 5.1 agrees with the process window as shown in Figure 5.2. In this case, examine the element distribution within the deposited layer becomes a necessity.

Table 5.1. Geometry of the single layers.

	Condition A (S355)	Condition D (S355)	Condition E (S355)	Condition D (AISI 420)
Energy input [J/mm]	101	127	151	129
Surface waviness [μm]	400	291	150	278
Maximum dilution [%]	12.18	18.05	20.32	19.60
Minimum dilution [%]	7.89	10.58	15.08	7.80

EDS scanning along the horizontal direction of the layer WAAM deposited Stellite 6 on S355 and AISI 420 steel substrates are performed and obtained results are shown in Figure 5.9. Various locations within the layer were examined. The scanning paths are selected in the transition zone between the adjacent beads so that any variation of the element content can be noticed directly. It shows in Figure 5.9 that Fe, Cr, Co, and W elements distributed relative uniformly, with fluctuation of 4.05%, 2.69%, 4.88%, and 5.85%, respectively. This result has a good match with the uniform microhardness observed and presented in Figure 5.10. The measured average microhardness of the deposited single bead (dashed line) is also plotted in Figure 5.10a together with the hardness profile of the deposited layers. It is noticed that the hardness of layers decreased slightly comparing to single bead average hardness. The smaller hardness reduction in the top clad layer may be due to the combined effect of changes in grain size and dilution of Fe [13,14]. The relative uniform hardness distribution in the horizontal direction (Figure 5.10b) indicated that the microstructure under overlapping condition is expected to be uniform.
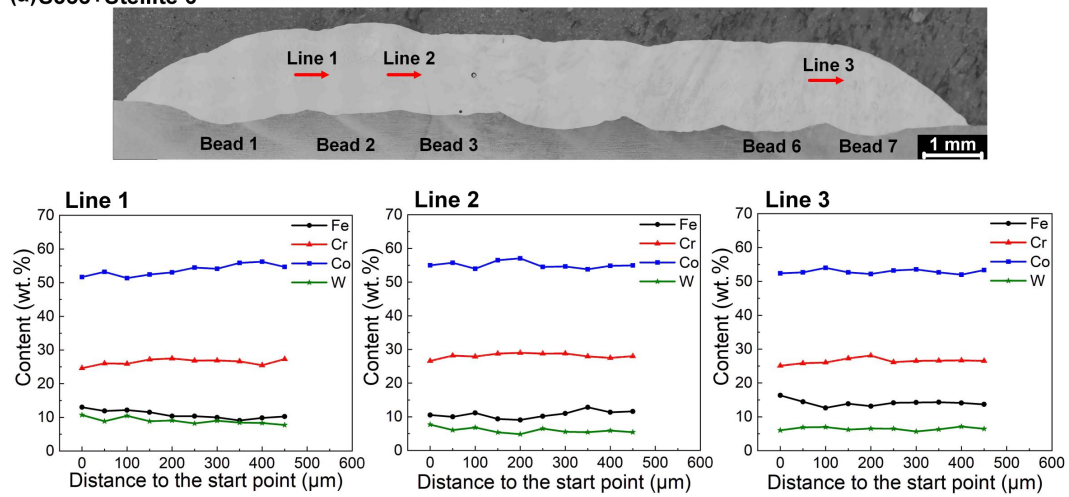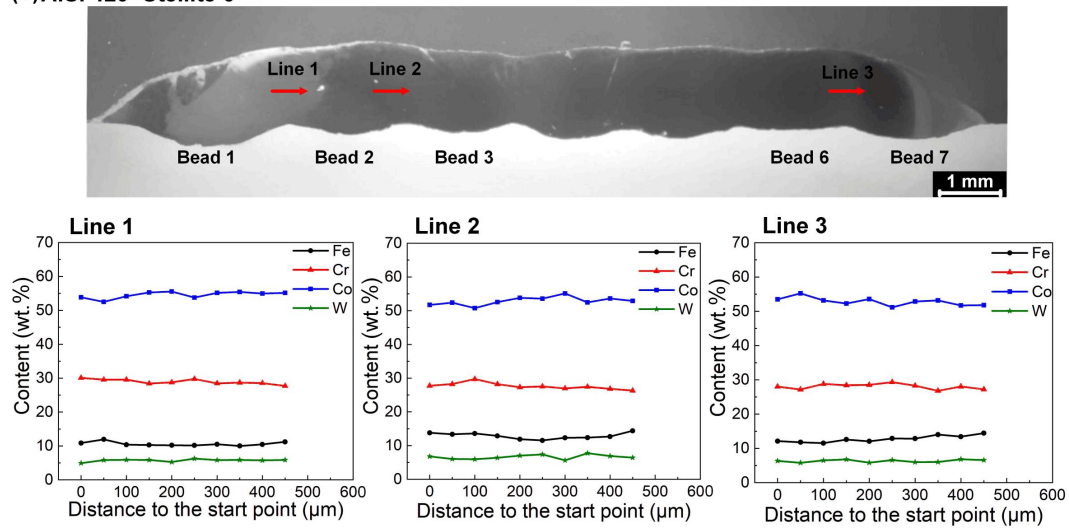
Figure 5.10 EDS examination along the horizontal direction of the WAAM deposited Stellite 6, (a) on S355 steel substrate; (b) on AISI 420 steel substrate.

The accumulative heat input introduced by the thermal cycles can promote the Fe dilution. However, as part of the arc energy is used to re-melt previous laid bead, this can lead to a melt depth reduction and a lower dilution. Eventually, a thermal balance can be reached, which maintain the dilution level between 10-20%. This indicates that the effect of thermal cycles on elements distribution is marginal when WAAM depositing Stellite 6 on steel substrates.
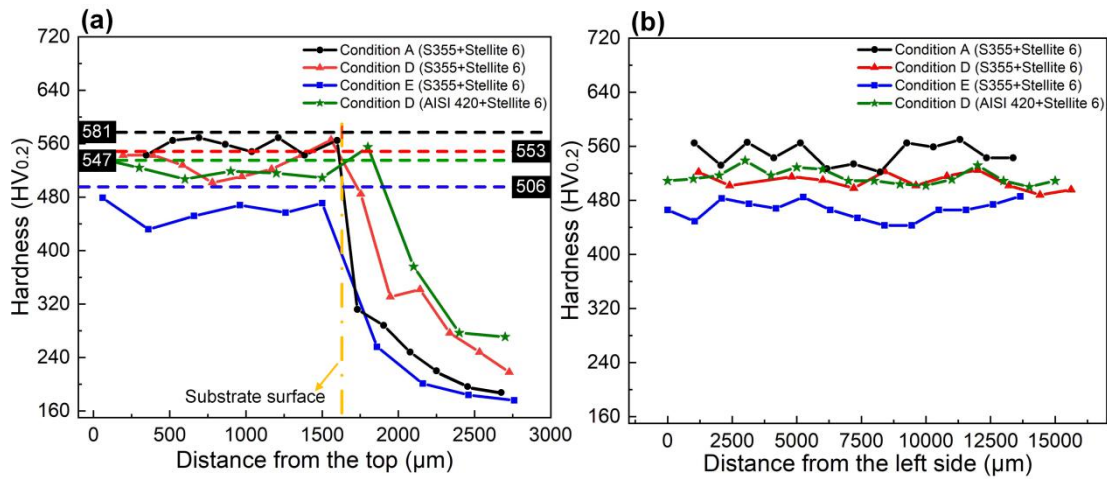
Figure 5.10 Hardness of the single layer, (a) Vertical direction; (b) Horizontal direction.

5.5 Phase identification of WAAM Stellite 6 on steel substrate

The XRD results in Figure 5.11 show that the FCC structure is Co-rich with elements such as Cr, Fe, etc. The Cr_7C_3 and Cr_3C_2 were identified as the carbides present in the deposits. The Co-rich carbides with W is identified as Co_4W_2C. Domalavage [19] suggests that a transformation from M_7C_3 to $M_{23}C_6$ would normally take place during aging. In this case, finer $M_{23}C_6$ secondary precipitated carbides will form to strengthen the matrix. However, in our study, even though Cr_7C_3 was found, the $Cr_{23}C_6$ carbide was not found in the WAAM deposited Stellite 6 layer.

Therefore, on one hand, these identified phases contribute to the wear and erosion properties of WAAM deposited Stellite 6 due to their high hardness. On the other hand, these Cr-carbides normally formed in the grain boundaries will harden the matrix through pinning up dislocations. The morphology, distribution, and size of the carbides will affect precipitation hardening effect, which will be the focus in our future research and is not further discussed here.
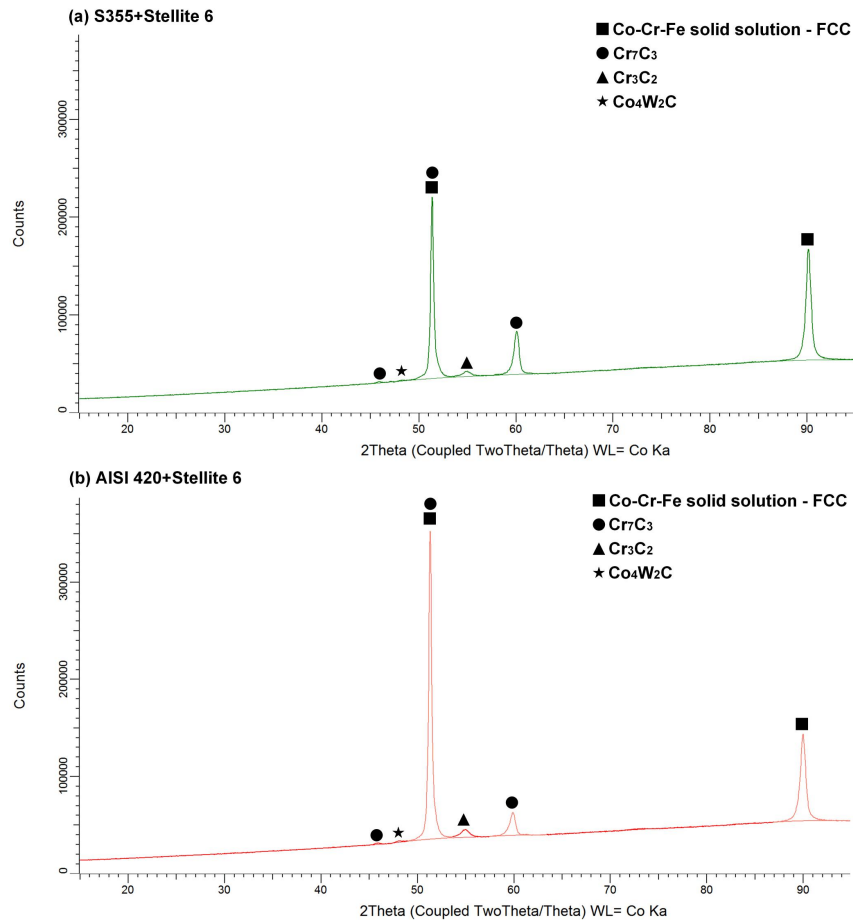
Figure 5.11 Phase identification of the WAAM deposited Stellite 6 on, (a) S355 + Stellite 6; (b) AISI 420 + Stellite 6.

5.6 Conclusions

WAAM depositing Stellite 6 on the different steel substrates was investigated in current research. Defect free Stellite 6 bead and layer were successfully deposited on both S355 and AISI 420 steel substrates with WAAM process. A processing window was established to guide the optimization of bead shape and dilution (geometrical). It was found in our study that a minimum heat input of 55 J/mm is needed to deposit a continuous bead. The increased heat input leads to grain growth and increased dilution, both of which can contribute to the hardness reduction. A heat input around 127 J/mm was found to be optimal for depositing the Stellite 6 without jeopardizing its hardness while maintaining a good surface finishing. Considering the surface waviness and dilution, the optimal overlap ratio was selected at 42%. The optimal deposition conditions based on S355 steel substrate can be adapted on the AISI 420 stainless steel substrate.

The EDS results in this study shown that the geometrical dilution may fail to represent element dilution. The hardness and EDS measurements, in perpendicular to welding direction and in the overlapping direction of the deposited layer, show uniform values. This indicates that thermal cycle introduced during multi-beads deposition has limited effects on the deposited layer. The XRD identifies the WAAM deposited Stellite 6

layer mainly contains Co-Cr-Fe solid solution with FCC crystal structure as matrix. The Cr_7C_3 and Cr_3C_2 are the carbides which can contribute to the strength and the identified Co_4W_2C carbides can contribute to the wear properties of the Stellite 6 WAAM deposits.

The findings of this research can provide a sound foundation for further exploring the wear properties of the WAAM deposited Stellite 6 layer. The limited effects of the thermal cycle on the element distribution and relative uniform bonding is promising for further development of a robust and automated WAAM deposition process, suitable for scale-up to industrial applications.

Bibliography

[1] de Oliveira U O B. Laser treatment of alloys: processing, microstructure and structural properties[M]. 2007.

[2] Ya W, Hernández-Sánchez J F, Pathiraj B, et al. A study on attenuation of a Nd: YAG laser power by co-axial and off-axial nozzle powder stream during cladding[C]//International Congress on Applications of Lasers & Electro-Optics. LIA, 2013, 2013(1): 453-462.

[3] Hashmi S. Comprehensive materials processing[M]. Newnes, 2014.

[4] Fan, Z & Jambunathan, A & Sparks, T.E. & Ruan, Jianzhong & Yang, Y & Bao, Yaxin & Liou, Frank. (2006). Numerical simulation and prediction of dilution during laser deposition. 17th Solid Freeform Fabrication Symposium, SFF 2006. 532-545.

[5] Schneider M F. Laser cladding with powder; Effect of some machining parameters on clad properties, University of Twente[D]. Ph. D Thesis, Enschede, The Netherlands, 1998.

[6] Ya W. Laser materials interactions during cladding: analyses on clad formation, thermal cycles, residual stress and defects[J]. 2015.

[7] Yan F, Xiong W, Faierson E. Grain structure control of additively manufactured metallic materials[J]. Materials, 2017, 10(11): 1260.

[8] Frenk A, Kurz W. Microstructural effects on the sliding wear resistance of a cobalt-based alloy[J]. Wear, 1994, 174(1-2): 81-91.

[9] Edmonds D V. The strengthening of an fe-vc low-alloy steel by carbide precipitation during continuous cooling from the austenitic condition[J]. Metallurgical Transactions, 1973, 4(11): 2527-2533.

[10] Rebouças Filho P P, da Silveira Cavalcante T, de Albuquerque V H C, et al. Measurement of welding dilution from images using active contours[C]//SEECCM 2009-2nd South-East European Conference on Computational Mechanics. 2009.

[11] Kumar S, Shahi A S. Effect of heat input on the microstructure and mechanical properties of gas tungsten arc welded AISI 304 stainless steel joints[J]. Materials & Design, 2011, 32(6): 3617-3623.

[12] Khromchenko F A, Lappa V A, Fedina I V, et al. Technology of repairing working blades of steam turbines. Part 1. Repair by the method of deposition of high-Cr alloys[J]. Welding international, 1999, 13(5): 405-408.

[13] Ferozkhan M M, Duraiselvam M, Ravibharath R. Plasma transferred arc welding of Stellite 6 alloy on stainless steel for wear resistance[J]. Procedia Technology, 2016, 25: 1305-1311.

[14] Kusmoko A, Dunne D P, Li H, et al. Deposition of Stellite 6 on nickel superalloy and mild steel substrates with laser cladding[J]. 2013.

[15] Ya W, Pathiraj B. Residual stresses in Stellite 6 layers cladded on AISI 420 steel plates with a Nd: YAG laser[J]. Journal of Laser Applications, 2018, 30(3): 032007.

[16] Xu, G., Kutsuna, M., Liu, Z., Yamada, K., 2006. Comparison between diode laser and tig cladding of Co-based alloys on the SUS403 stainless steel. Surface and Coatings Technology 201 (3), 1138–1144.

[17] Silwal B, Walker J, West D. Hot-wire GTAW cladding: inconel 625 on 347 stainless steel[J]. The International Journal of Advanced Manufacturing Technology, 2019: 1-10.

[18] Valsecchi B, Previtali B, Gariboldi E. Fibre laser cladding of turbine blade leading edges: the effect of specific energy on clad dilution[J]. International Journal of Structural Integrity, 2012, 3(4): 377-395.

[19] Yangtao X, Tiandong X, Yanling H. Microstructures comparison of Stellite 6 alloy by self-propagating high-temperature synthesis and cast HS111 alloy[J]. Rare Metal Materials and Engineering, 2009, 38(8): 1333-1337.

3D modelling of single-bead WAAM deposition

Mass and energy conservation equations are the basic principle of the model. The mass-energy balance is solved with the aid of the finite element software COMSOL Multiphysics® 5.3. The geometries of a single AM-XC-45 bead are calculated as a function of the processing parameters. The progressive formation of the deposit is solved with a moving mesh branch in COMSOL. The coupled model takes into account the mass addition and phase changes between melt and solid as well as the changes in thermal properties with temperature. Surface tension and the Marangoni effects were excluded due to the difficulty in simulating the wire feeding. The temperature distributions were calculated with the solid heat transfer branch in COMSOL. The developed model is described in detail in the following sections.

6.1 Governing equations

The mass-energy balance Eq. (6-1) is expressed as,

$$\rho_b C_{\mathrm{p}} \frac{\partial T}{\partial \mathrm{t}} + \rho_w C_p v_{\mathrm{b}} \frac{\partial T}{\partial \mathrm{y}} = \nabla \cdot (k \nabla T) + Q_{\mathrm{abs}} - Q_{\mathrm{loss}} \quad (6\text{-}1)$$

where ρ_b and ρ_w are the density of base and wire materials (kg m^{-3}). C_p is the equivalent heat capacity of base and wire materials (J kg^{-1}K^{-1}). T is the temperature (K) and v_b is the speed of moving boundary (m s^{-1}). k is the thermal conductivity of base and wire materials (W m^{-1}K^{-1}), Q_{abs} is the energy absorbed by wire and base material (W m^{-3}). Q_{loss} is the energy lost into room air by thermal radiation and convection and by heat conduction with the work table (W m^{-3}).

6.1.1 Heat source

In this research, a body heat source in double-ellipsoidal distribution was applied on the base, and the distribution of the heat flux is described, as Eq. (6-2):

$$Q_{front} = q_{max} \exp^{-3\left[\frac{(x-x_{00})^2}{(a)^2} + \frac{(y-y_{00})^2}{(c_f)^2} + \frac{(z-z_{00})^2}{(b)^2}\right]} \quad (x >= x_{00})$$

$$Q_{rear} = q_{max} \exp^{-3\left[\frac{(x-x_{00})^2}{(a)^2} + \frac{(y-y_{00})^2}{(c_r)^2} + \frac{(z-z_{00})^2}{(b)^2}\right]} \quad (x < x_{00})$$

$$q_{max} = \frac{UI\mu 6\sqrt{3} f_r}{abc_r \pi \sqrt{\pi}} = \frac{UI\mu 6\sqrt{3} f_f}{abc_f \pi \sqrt{\pi}}$$

$$f_f + f_r = 2$$

$$f_f / c_f = f_r / c_r$$

$$f_f = \frac{c_f}{c_f + c_r}$$

$$(6\text{-}2)$$

where q_{max} is the maximum heat flux of arc (W m^{-3}). (x_{00}, y_{00}, z_{00}) is the arc center (m). Q_{front} is heat distribution inside the front quadrant (W m^{-3}), Q_{rear} is heat distribution inside the rear quadrant (W m^{-3}). a, b, c_r, and c_f are the character parameters of arc heat source (m). U, I, and μ are voltage (V), current (A), and arc efficiency (0.9 in this study). The schematic of double-ellipsoidal heat source is shown in Figure 6.1. The deposit geometry produced during WAAM deposition is strongly influenced by the temperature distribution [1]. Temperature distributions are essentially determined from the energy absorbed (Q_{abs}) by the base and molten wires.
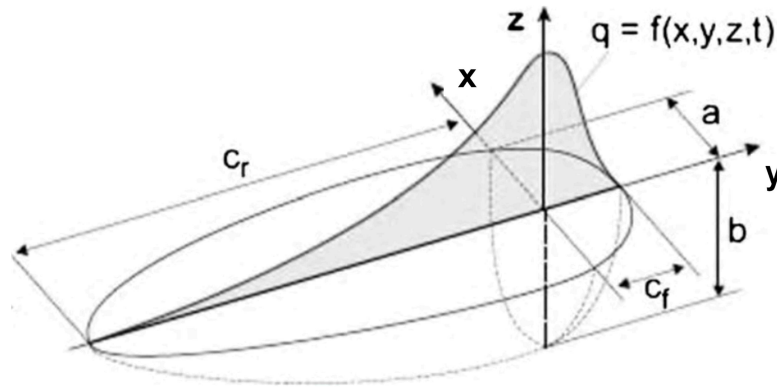
Figure 6.1 The schematic of double-ellipsoidal heat source [2].

6.1.2 Physical properties of materials
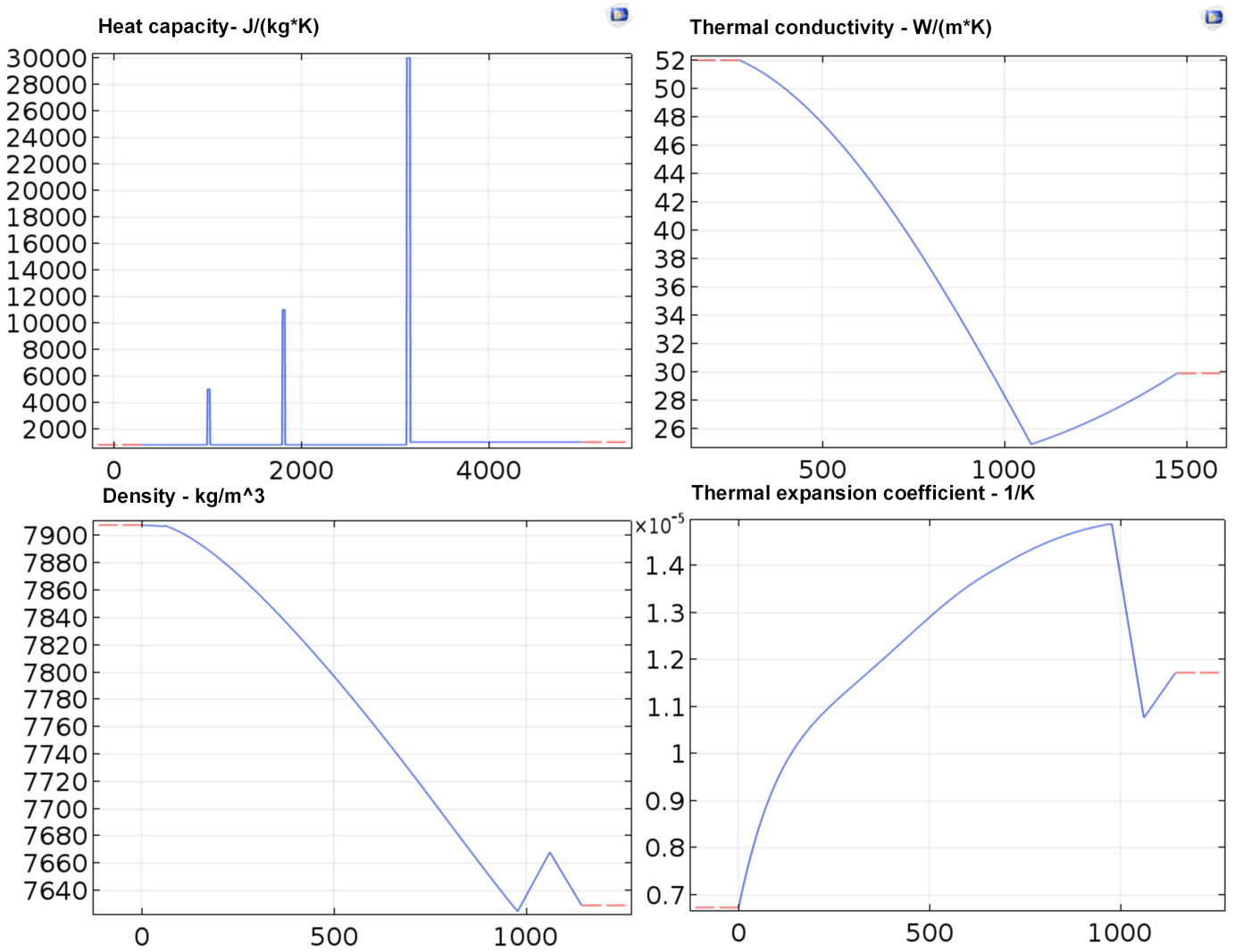
Figure 6.2 The related thermodynamic parameters used in this study [3-5].

Latent heat is taken into account as equivalent heat capacity (C_p) and can be described as Eq. (6-3),

$$C_p(T) = C_{p_m}(T) + \frac{\Delta H_m}{(T_m - T_0)} \quad (6\text{-}3)$$

where T_m is the melting point (K), T_0 is the room temperature (298 K) and ΔH_m is the latent heat of fusion (J kg^{-1}). C_{pm} (T) is the heat capacity of base and wire materials (J kg^{-1}K^{-1}). The related thermodynamic parameters used in this study is output from the database of COMSOL Multiphysics® 5.3 and shown in Figure 6.2. These parameters were also used by other researchers and studies [3-5].

6.1.3 Boundary conditions
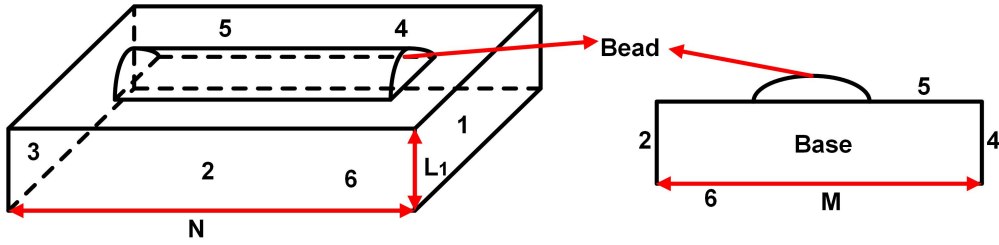
Figure 6.3 The schematic overview of the boundaries.

During the deposition operation, the base and bead exchange heat with the surrounding environment by convection and conduction. The schematic overview of the boundaries is shown in Figure 6.3. The convection condition of side surface 1-4 of base is shown in Eq. (6-4) and (6-5),

$$Q_{convection} = h_{convection}(T - T_0) \quad (6\text{-}4)$$

$$h_{convection} = h_{air}(L_1, P_a, T_0) \quad (6\text{-}5)$$

where L_1 is the thickness of base (m), P_a is standard atmospheric pressure (P_a), $h_{convection}$ is natural heat convection coefficient of air (W m^{-2} K^{-1}), and $Q_{convection}$ is the natural convection heat flux of surface 1-4 (W m^{-2}). The top surface 5 of base is also considered to experience natural heat convection but the bead region is considered to be in forced convection during deposition. So, the corresponding boundary conditions are established as:

$$Q_{convection'} = h_{connection'}(T - T_0) \quad (6\text{-}6)$$

$$h_{convection'} = h_{air}(L_2, v_{air}, P_a, T_0) \quad (6\text{-}7)$$

$$L_2 = \frac{M \cdot N}{2M + 2N} \quad (6\text{-}8)$$

where $h_{convection'}$ is forced heat convection coefficient of air (W m^{-2} K^{-1}), L_2 is effective length of base, determined by base width (M) and length (N), (m), $Q_{convection'}$ is forced heat convection heat flux (W m^{-2}), v_{air} is flow rate of air during deposition (m s^{-1}). Finally, the bottom surface 6 of base experience heat conduction between worktable and base. The relationship can be set up as:

$$Q_{conduction} = h_t(T - T_0) \quad (6\text{-}9)$$

where h_t is the heat conduction coefficient of worktable (W m^{-2} K^{-1}), $Q_{conduction}$ is the conduction heat flux via worktable (W m^{-2}). Therefore, the total heat loss Q_{loss} shown in Eq. (6-1) is the sum of the heat loss as heat convection with ambient air and heat conduction with the worktable (W m^{-2}), as shown in Eq. (6-10).

$$Q_{loss} = Q_{convection} + Q_{convection'} + Q_{conduction} \quad (6\text{-}10)$$

6.1.4 The deposition progress
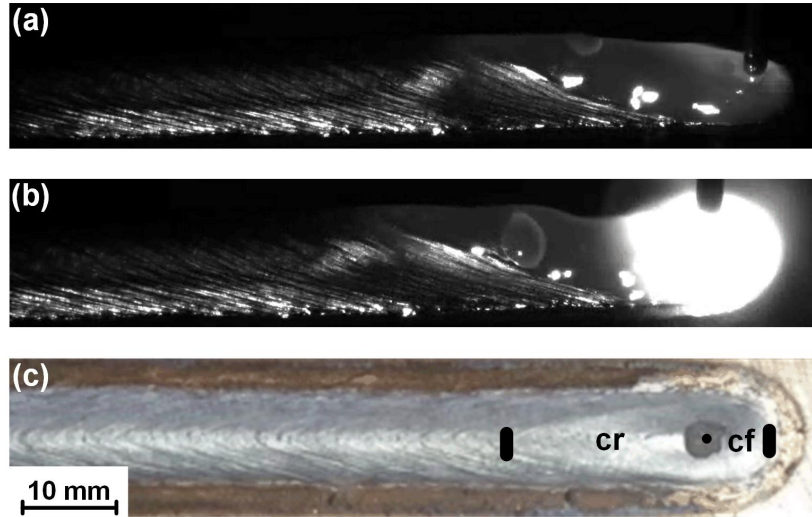
Figure 6.4 (a), (b) molten pool during deposition; (c) bead appearance after deposition.

Based on the picture of molten pool taken during the deposition process as shown in Figure 6.4a and 6.4b and the final bead appearance as shown in Figure 6.4c, it can be seen the range of molten pool. This observation can be used to define the start and the end point of bead height growth in the model. The time period of this range is interaction time of molten pool (t_{in}).
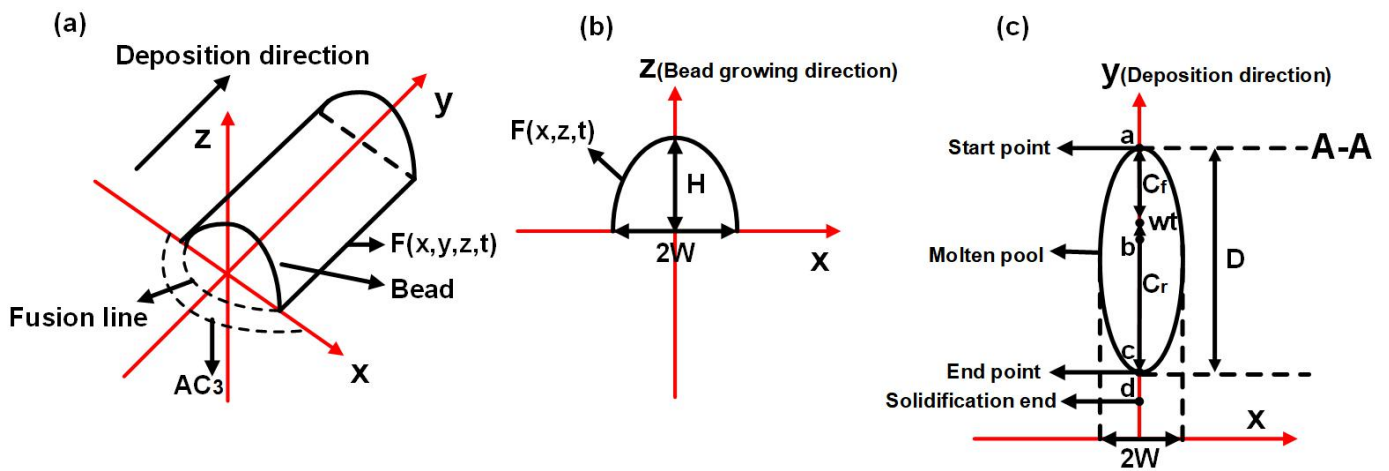
Figure 6.5 (a) bead geometry in 3D; (b) bead geometry in x-z plane; (c) the schematic overview of bead height growth.

Figure 6.5a shows the bead geometry in 3D, so that function F_0 (x, y, z, t) represents a single bead geometry in 3D. In a 2D model case, this function F_0 (x, y, z, t) is reduced to F_0 (x, z, t), which represents the changes of bead width and height during the deposition process (Figure 6.5b). The derivative of the F_0 over time is the velocity of moving boundary (v_b, top surface of the base) speed due to the wire addition. v_b can be calculated using the following expression,

$$v_b = \frac{F_0(x,z,t)}{dt} \quad (6\text{-}11)$$

The boundary moving conditions are, i) the boundary only moves within the interaction time (t_{in}), and ii) the v_b is considered equal to zero when the temperature is below the melting point of the deposition material.

Most of the cross sections of the single bead profile quoted in literature [6] are summarized as a parabolic shape when a double-ellipsoidal distributed heat source is used. In Figure 6.5b, the parabolic function used to approximate the bead geometry in the model is,

$$F_0(z) = a_0 x^2 + b_0 x + c_0 \quad (6\text{-}12)$$

The mass balance governs the geometry of model, which is assumed to be constant when depositing single bead, so for single bead, the equations are,

$$
\begin{aligned}
F_0 &= a_0 x^2 + b_0 x + c_0 \\
F_0(W) &= F_0(-W) = 0 \quad (6\text{-}13) \\
F_0(0) &= H
\end{aligned}
$$

where a_0, b_0, and c_0 are the coefficient used to define the geometry of the single bead.

Figure 6.5c shows the formation process of the bead. The molten droplets transfer from the position in front of the wire tip (point a in Figure 6.5c) to the molten pool, which indicates the start of bead height growth. when the heat source moves away, the bead height growth stops (point c in Figure 6.5c). The two points are corresponding and matching with the experimental result as shown in Figure 6.4c. Therefore, the time of bead height growth (interaction time, t_{in}) at a specific position (cross section) can be defined as:

$$t_{in} = \frac{D}{v} \quad (6\text{-}14)$$

where D is the distance between points a and c (m), v is deposition speed (m s^{-1}).

To summarize the assumptions used to develop the model are as following,

(a) The heat source is assumed to be double-ellipsoidal.

(b) Latent heat was integrated into the heat capacity.

(c) The spatter and vaporization of materials was neglected. Hence, all the filler materials are considered to be transferred into molten pool.

(d) Heat transfer only considered conduction from base, natural convection by air. Other factors like heat loss caused by flow of shielding gas were not considered.

(e) Bead profile was assumed to be in parabolic shape.

(f) The surface tension between the substrate and molten pool was not considered.

6.2 Results and discussion

The parameters used in simulation is shown in Table 6.1.

Table 6.1 The simulation and experimental parameters used in this study.

Parameters	Description	Units	Value
μ	Heat transfer coefficient of GMAW arc	/	0.9
U	Voltage	[V]	15.6
I	Current	[A]	240
v	Deposition speed	[m min^{-1}]	1
k	Thermal conductivity of material	[W m^{-1} K^{-1}]	Figure 6.2
ρ	Density of material	[kg m^{-3}]	Figure 6.2
Cp	Specific heat of material	[J kg^{-1} K^{-1}]	Figure 6.2
(x_0, y_0, z_0)	Start point of arc	[m]	(0,0,0)
H	Height of bead	[m]	0.00167
W	Half width of bead	[m]	0.00321
T_0	Room temperature	[K]	298
a	Arc width	[m]	0.007
b	Arc penetration depth	[m]	0.001
c_f	Arc front length	[m]	0.005
c_r	Arc rear length	[m]	0.015
L	Bead length	[m]	0.1
t_{in}	Interaction time	[s]	1.2
P	Pressure	[MPa]	0.101
σ	Thermal expansion coefficient	[1/K]	Figure 6.2
v_w	Wire feed speed	[m min^{-1}]	6.5
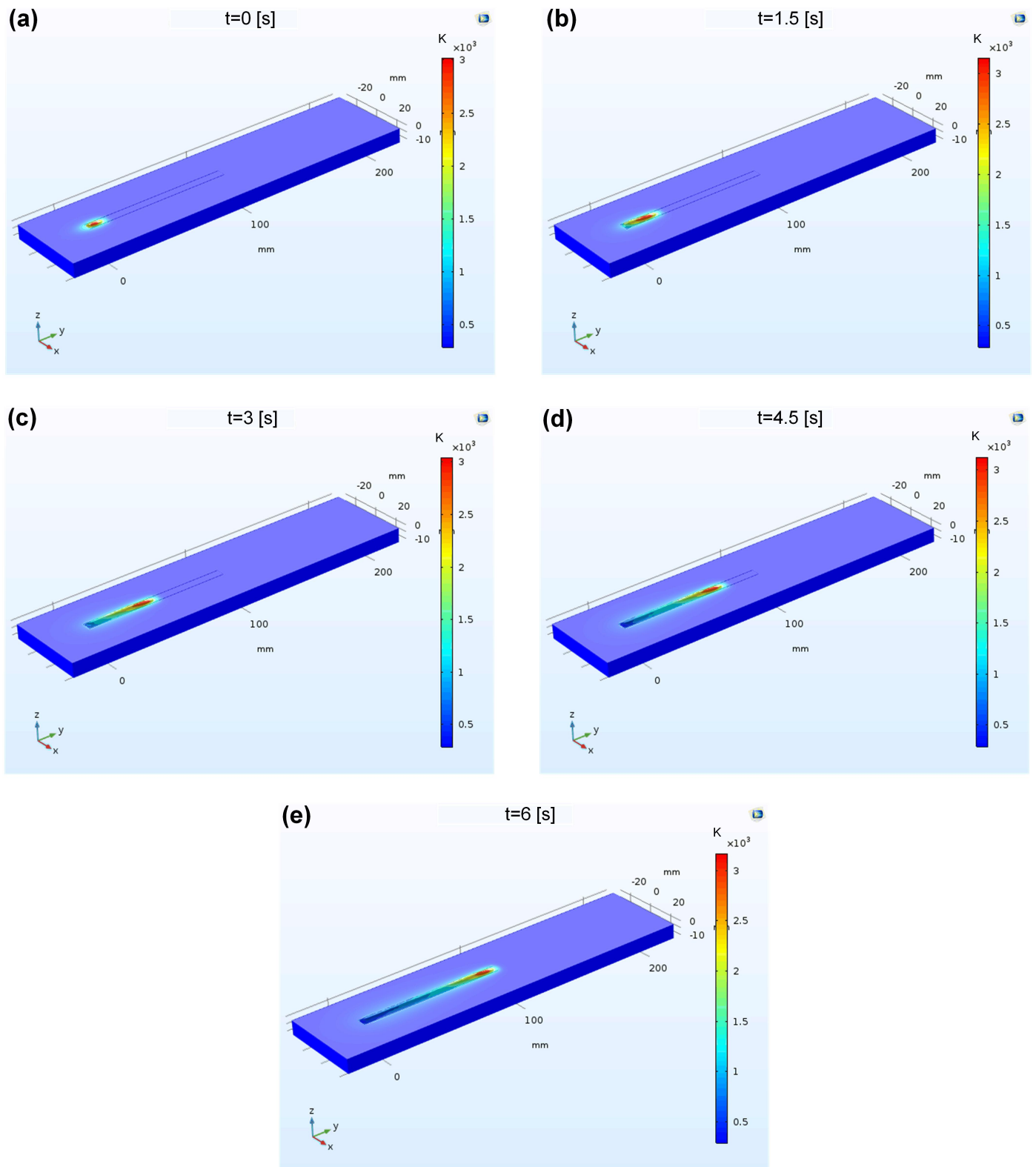
Figure 6.6 The overview of temperature distribution and bead profiles at different time points, (a) t=0 s; (b) t=1.5 s; (c) t=3 s; (d) t=4.5 s; (e) t=6 s.

The simulated single bead deposition result is shown in Figure 6.6. From Figure 6.6a to 6.6e, it shows the deposition progress at different time. The mass, and energy transfers together with the geometry of the bead were computed in the coupled manner. It shows the progress of WAAM deposition including temperature

distribution and deposited materials. As the moving mesh technique was used in the modelling, the freshly generated meshes represent the deposited material [6]. This is also indicated in Figure 6.6.
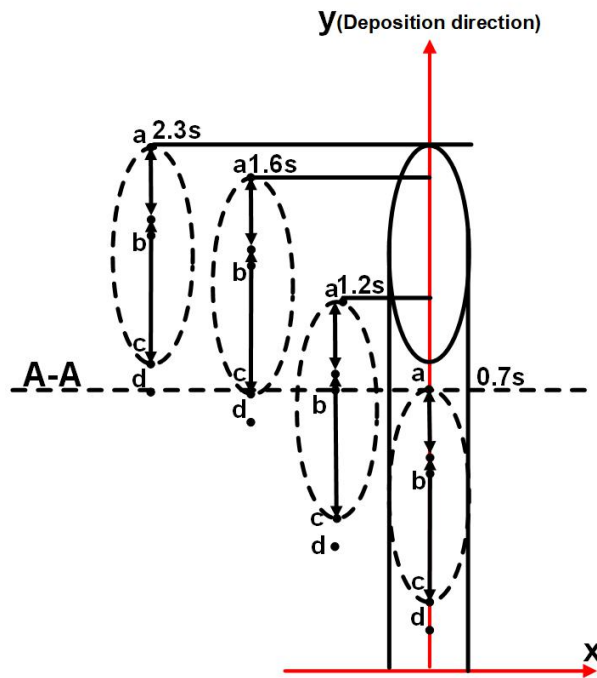
Figure 6.7 The schematic overview of bead formation.
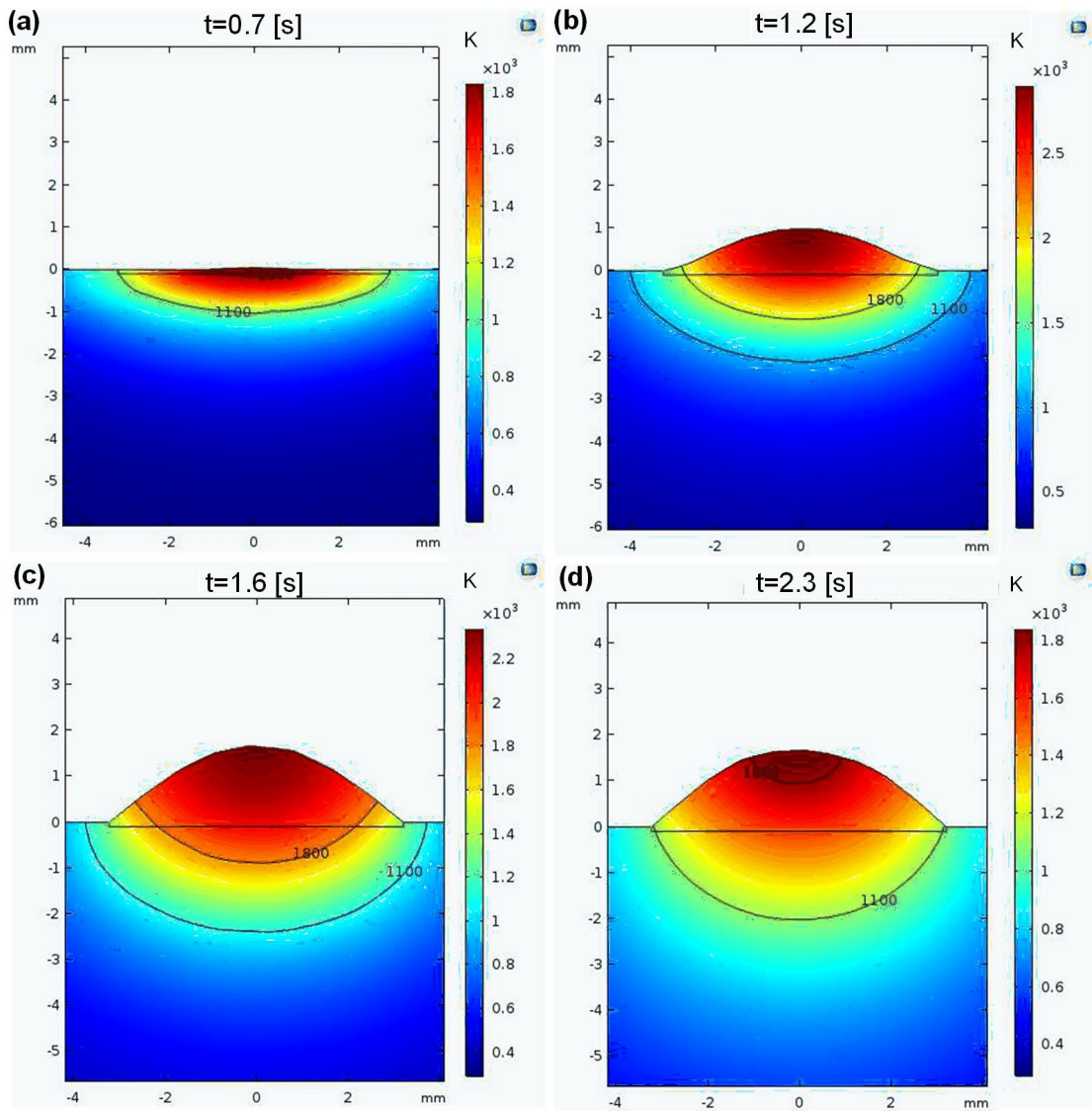
Figure 6.8 The temperature distribution and bead profiles of the cross section at different time points, (a) t=0.7 s; (b) t=1.2 s; (c) t=1.6 s; (d) t=2.3 s.
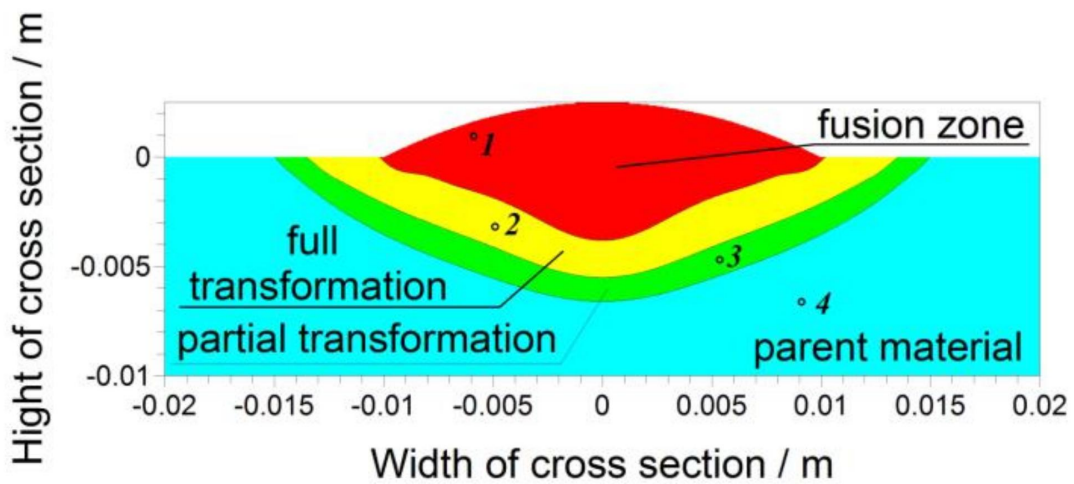
Figure 6.9 The cross section of welded S355 steel [7].

In order to trace the deposition process, a 2D cross section was extracted from the simulated 3D model as showing in Figure 6.6. It is the position as shown in Figure 6.7 (cross section A-A). The deposition progress of such cross section is shown in Figure 6.8. It shows that the bead starts growing at the t=0.7 s (Figure 6.8a), when the materials starts to melt. It is indicated as the point a shown in Figure 6.7. At t=1.2 s (Figure 6.8b), it reaches the highest temperature of the molten pool where the wire tip (point w_t) just past the selected cross section A-A. Figure 6.9 shows the welded S355 steel cross section, from which the position of fusion line (between zone 1 and 2) and A_1 lines (between zone 3 and 4) can be found [7]. By tracing the position of the melting temperature and A_1 temperature at this point in time from the simulated isotherms, the dilution and HAZ are determined [6]. It is corresponding to point b in Figure 6.7. The characteristic temperature lines including fusion line (1800 K) and A_1 (1100 K) are shown in Figure 6.8. From the time t=1.2 s to t=1.6 s, the heat source moves away from the cross-section A-A. While the heat source still has the heating effect on the cross section A-A, cooling becomes dominant. Therefore a reduction of the temperature was observed. From Figure 6.8b to 6.8c, the fusion line moves up, indicating a cooling process indeed. During this time period (t=1.2 s to t=1.6 s), the temperature is still higher than the melting point, meaning that the deposited material is still at the liquid state. During this process, it is expected that the bead keeps growing mainly through the molten droplets flowing from the front to the back of the arc until the bead height growth finishes at t= 1.6 s. This is also indicated in Figure 6.7 as the dashed ellipse point c just moved across the cross-section A-A. Finally, the materials solidify at t= 2.3 s (Figure 6.8d). This corresponds to point d moved to cross section A-A (Figure 6.7). This is different than when the heat source is a laser spot, for which the interaction time is simply the laser spot size divided by the cladding speed. In our case, the cooling rate during the WAAM process is lower than the laser. Hence, the three stages of material addition are defined in this study to represent the deposition process.
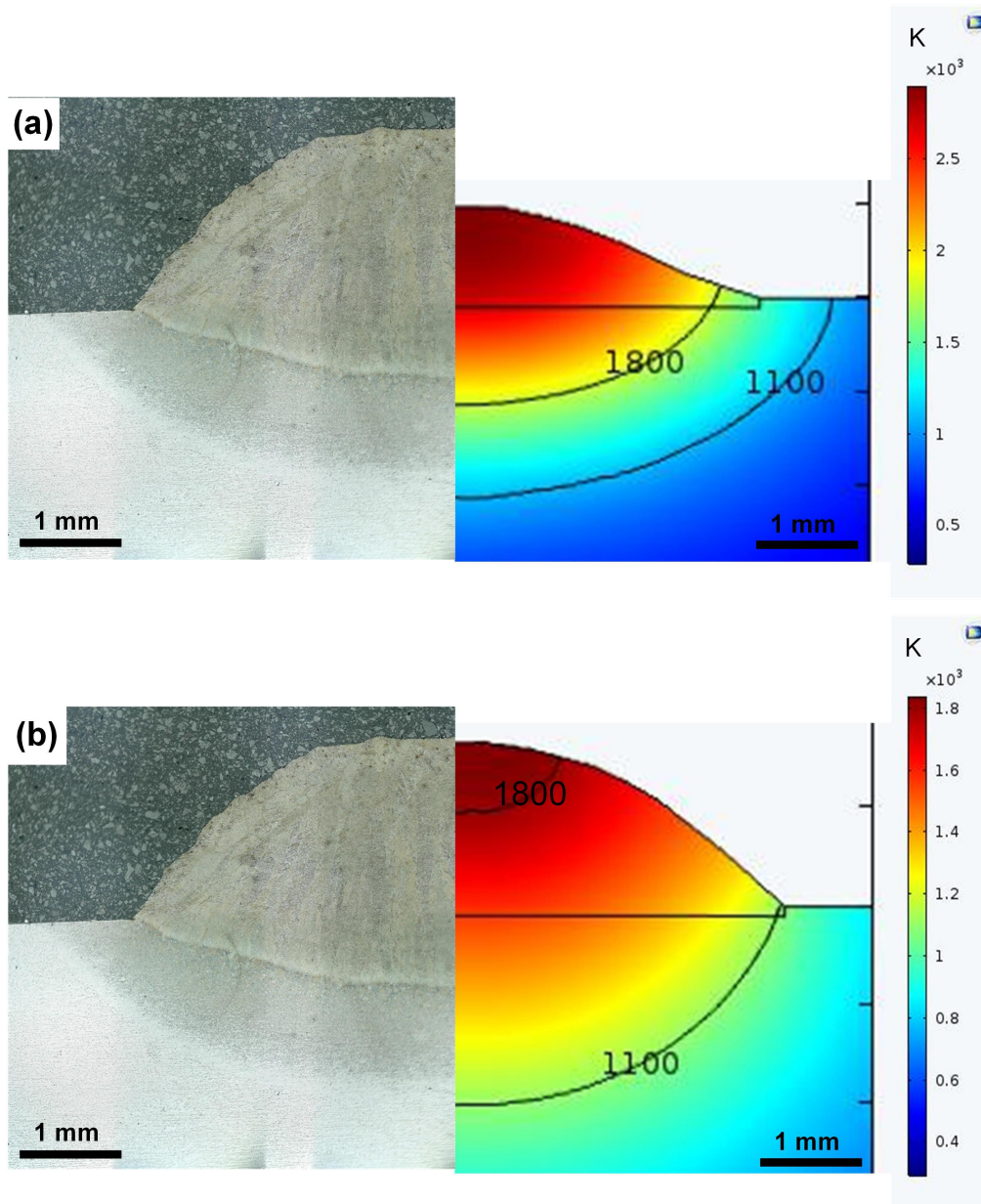
Figure 6.10 The comparison of the simulated cross section and experimental cross section, (a) fusion line; (b) bead geometry and A_1 temperature.

The simulated and experimental cross section is compared and shown in Figure 6.10. It is shown that the fusion line (1800 K) in the simulated result has some deviation compared to the experimental value. It may be because the molten pool flow introduced convection of the heat was neglected. The simulated A_1 temperature line shows a good agreement with the experimental value.

Through the numerical and experimental studies, it was found that there are physical differences in material and heat transfer between WAAM and laser depositions. During the WAAM process, the material addition progress is found to take place in three stages for a selected cross section, including bead height growth + temperature increasing stage, bead height growth + temperature decreasing stage, and bead constant + temperature decreasing stage. Therefore, it can be seen that the WAAM deposition is comparably more

complex than the laser-based AM process which has fewer stages. Although the moving mesh technique can be applied for simulating WAAM deposition and provides reasonable results, more details should be included such as phase transformations, molten pool flow, etc.

This model is used to simulate the bead geometry and the temperature distribution during the single bead on plate deposition. The simulation frame work can be used with the appropriate adaptation of the boundary conditions for multiple-bead depositions, either in height or in layer form.

6.3 Conclusions

This chapter introduces a simple single bead model for WAAM deposition, based on the preliminary simulated and the experimental results, the following conclusions can be drawn,

(a) The dilution and HAZ of the WAAM single bead can be simulated. The A_1 line agrees with experimental result.

(b) The material addition progress is divided into three stages including the points b, c, and d moving across the cross-section A-A as shown in Figure 6.7. The WAAM deposition is comparably more complex than laser process due to the relative low cooling rate.

(c) Although moving mesh technique can be applied for simulating WAAM deposition and providing good results, more detailed research should be included such as phase transformation, molten pool flow, etc. This is beyond the scope of the master thesis but it would be interesting to explore in the future.

Bibliography

[1] Dowden, J., 2009. The Theory of Laser Materials Processing: Heat and Mass Transfer in Modern Technology. Vol. 119. Springer Science & Business Media.

[2] Jia X, Xu J, Liu Z, et al. A new method to estimate heat source parameters in gas metal arc welding simulation process[J]. Fusion Engineering and Design, 2014, 89(1): 40-48.

[3] Hendri Y, Jaharah A G, Che H C H. Machining Simulation of AISI 1045 and Carbide Tool Using FEM[J]. 2008.

[4] Gopal, Arunkumar. (2018). DESIGN AND OPTIMIZATION OF CRANKSHAFT FOR SINGLE CYLINDER 4 – STROKE SPARK IGNITION ENGINE USING COUPLED STEADY-STATE THERMAL STRUCTURAL ANALYSIS.

[5] Zamiri F, Drezet J M, Nussbaumer A. Welding simulation of tubular K-joints in steel S690QH[C]//Tubular Structures XV: Proceedings of the 15th International Symposium on Tubular Structures, Rio de Janeiro, Brazil, 27-29 May 2015. CRC press, 2015: 481.

[6] W. Ya, B. Pathiraj, S. Liu, 2D modelling of clad geometry and resulting thermal cycles during laser cladding, Journal of materials processing technology 230 (2016) 217-232.

[7] Winczek J, Gawronska E, Gucwa M, et al. Theoretical and Experimental Investigation of Temperature and Phase Transformation during SAW Overlaying[J]. Applied Sciences, 2019, 9(7): 1472.

7

Conclusions and Recommendations

7.1 Conclusions

Base on the current work, some important conclusions and findings can be drawn as follows,

● The mechanical properties of the WAAM deposited steel part using AM-XC-45 metal-cored are comparable or superior to the traditional process, which means that is has a good potential for utilisation of metal-cored wires in WAAM.

● The hardness profile observed in our experiments is different from the literature [1,2], which can be related to the high carbon content and the low microalloying elements composition which dictated the mechanical behavior.

● The Stellite 6 was successfully deposited using WAAM. The dilution and hardness of the deposit can reach the same level as laser deposition. The increased heat input leads to grain growth and higher dilution which can cause hardness reduction.

● The optimal deposition condition of Stellite 6 using WAAM on the S355 mild steel can be transferred to AISI 420 stainless steel.

● In our study, it is found that the geometrical dilution fails to represent the chemical dilution, which is different with the finding obtained from previous literatures.

● The WAAM deposited Stellite 6 layer mainly contains Co-Cr-Fe solid solution with FCC crystal structure as the matrix. The Cr_7C_3 and Cr_3C_2 are the carbides which can contribute to the strength and the identified Co_4W_2C carbides can contribute to the wear properties of the Stellite 6 WAAM deposits.

● A simple single bead model was established. The temperature distribution and dilution can be simulated with this model.

7.2 Recommendations

- The deposited AM-XC-45 part shows undesirable elongation, indicating that further post heat treatment is required to improve the ductility of the part.

- With the optimal condition, the wear property of the WAAM deposited Stellite 6 can be further explored for industrial applications.

- For improving the modelling of the WAAM deposition process, more detailed research work can be added on the developed model with the addition of phase transformation, molten pool flow, strain/stress distribution, etc.

Bibliography

[1] Rodrigues T A, Duarte V, Avila J A, et al. Wire and arc additive manufacturing of HSLA steel: Effect of thermal cycles on microstructure and mechanical properties[J]. Additive Manufacturing, 2019, 27: 440-450.

[2] Haden C V, Zeng G, Carter III F M, et al. Wire and arc additive manufactured steel: Tensile and wear properties[J]. Additive Manufacturing, 2017, 16: 115-123.